Supplementary Information
Taming the nucleation and growth kinetics of lead halide perovskite quantum dots

Quinten A. Akkerman,[1,2] Tan P. T. Nguyen,[3] Simon C. Boehme,[1,2] Federico Montanarella,[1,2] Dmitry N. Dirin,[1,2] Philipp Wechsler,[1] Finn Beiglböck,[2] Rolf Erni,[4] Claudine Katan,[3] Jacky Even[5] and Maksym V. Kovalenko[1,2]

[1]Department of Chemistry and Applied Biosciences, ETH Zürich, Zürich CH-8093, Switzerland

[2]Empa-Swiss Federal Laboratories for Materials Science and Technology, Dübendorf, CH-8600, Switzerland

[3]Univ Rennes, ENSCR, INSA Rennes, CNRS, ISCR - UMR 6226, F-35000 Rennes, France

[4]Electron Microscopy Center, Empa – Swiss Federal Laboratories for Materials Science and Technology, Dübendorf, Switzerland.

[5]Univ Rennes, INSA Rennes, CNRS, Institut FOTON - UMR 6082, F-35000 Rennes, France

Supplementary Note 1. Additional details for synthesis and data analysis.

1.1. Synthesis details and parametric screening

The QD size in this work was mainly regulated by changing the overall concentration (dilution) or by adjusting the concentration of TOPO, as described in the main text. In addition, the size could be controlled also by varying the concentration of $PbBr_2$ and Cs-DOPO individually. **Supplementary Fig. 1** illustrates the effect varying the quantity of the $PbBr_2$ stock solution (with a fixed $PbBr_2$:TOPO ratio and fixed amount of injected Cs-DOPA solution). Larger QDs were obtained at higher $PbBr_2$ concentrations. Alternatively, keeping the $PbBr_2$ fixed and decreasing the amount of injected Cs-DOPA results in a similar trend within a Pb:Cs ratio of 2-8, wherein higher Cs-DOPA concentration result in larger QDs, as shown in **Supplementary Fig. 2**. Above the 8:1 Pb:Cs ratio, the concentration of Cs-DOPA does not seem to alter the final size of the QDs. Decreasing the Pb:Cs ratio to below 2:1 will lead to the formation of the Cs_4PbBr_6 phase, as is evident from the strong absorption around 3.95 eV, as shown in **Supplementary Fig. 3**. Finally, the increase of the DOPA concentration in the Cs-DOPA precursor, and therefore the increase of free DOPA ligands during the reaction, does not have a significant effect on the final size and growth speed of $CsPbBr_3$ QDs, as shown in **Supplementary Fig. 4**. The reproducibility of this room-temperature $CsPbBr_3$ synthesis is illustrated in **Supplementary Fig. 5**, wherein a specific reaction is repeated four times (800 µl $PbBr_2$ stock solution, 50 µl Cs-DOPA stock solution and 5000 µl hexane). All four reactions yield the same growth curve, with a standard deviation in the final size of just 2%. Similar values are found for the peak FWHM and the PL peak position.

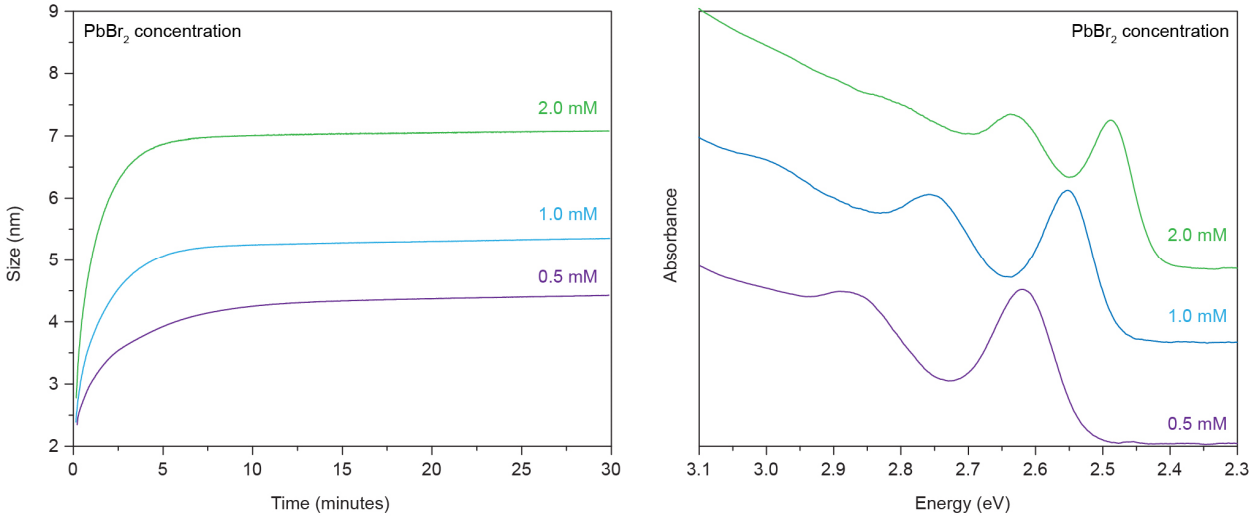

Supplementary Fig. 1 | $CsPbBr_3$ QD size-control by varying the $PbBr_2$ precursors with a fixed Cs-DOPA concentration, showing larger QDs and faster reactions with increasing $PbBr_2$ concentration.

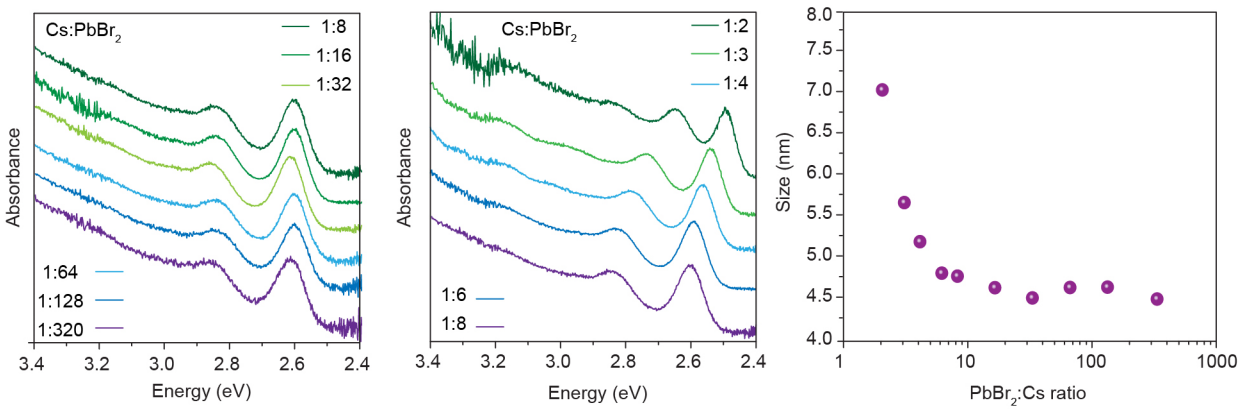

Supplementary Fig. 2 | Effect of Cs:Pb molar precursor ratio, showing no effect on the QD size at very large Pb excess, and a convenient size-tuning for ratios between 1:8 and 1:2.

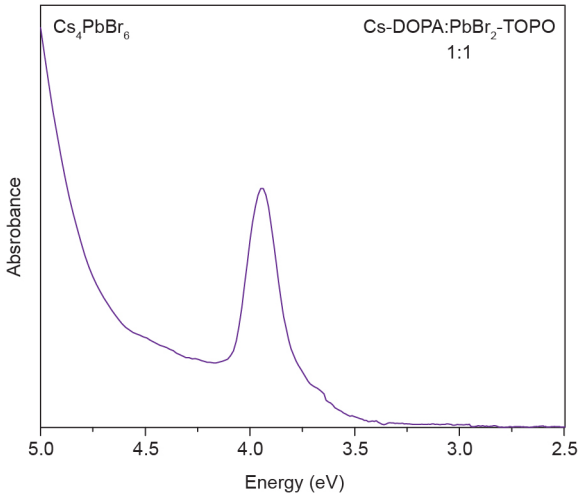

Supplementary Fig. 3 | Formation of Cs_4PbBr_6, characterized by the narrow absorption at 3.95 eV[1], at a Cs to Pb ratio of 1:1.

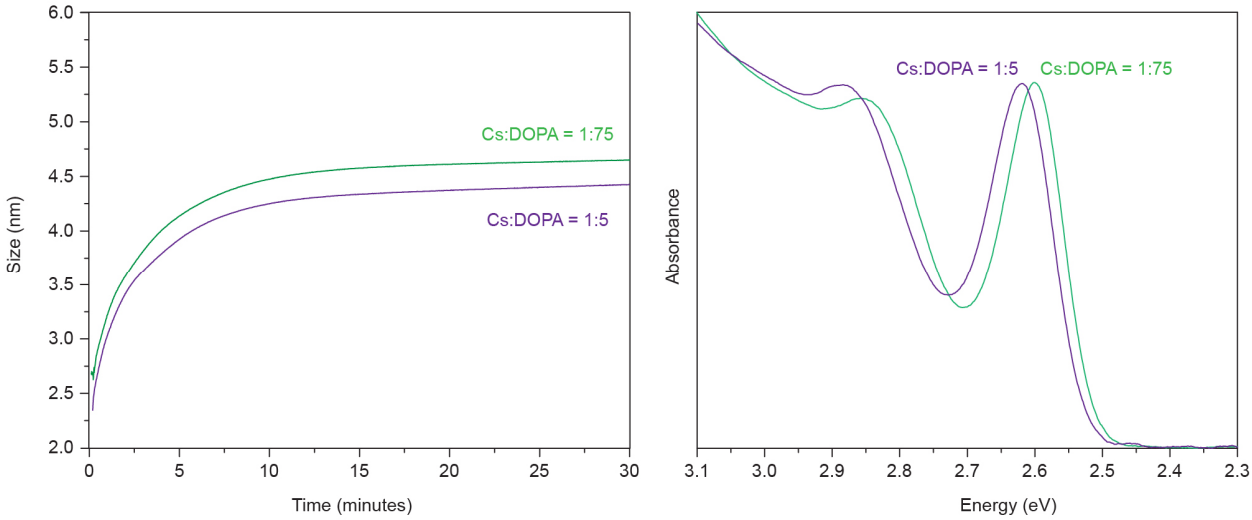

Supplementary Fig. 4 | Experiments with the high excess of DOPA acid, with keeping all other reaction conditions fixed, demonstrating that excess DOPA does not influence the growth of $CsPbBr_3$.

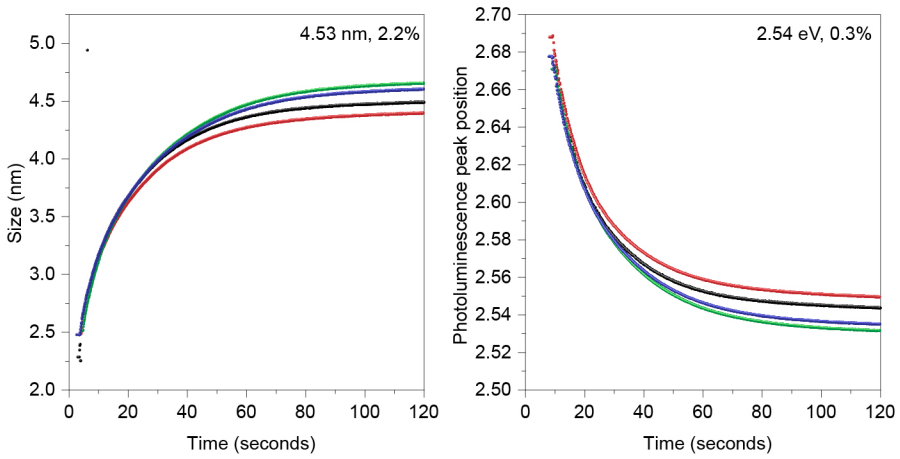

Supplementary Fig. 5 | Reproducibly of $CsPbBr_3$ QD synthesis confirmed by repeating the same synthesis four times.

1.2. *In-situ* data analysis

Due to the large number of spectra (> 1000 per synthesis), Python scripts were used to extract absorption peak positions, first absorption peak FWHM, as well as PL peak positions and FWHM. The first absorption peak position and its respective FWHM were smoothed (Savitzky–Golay) and fitted with a partial Gaussian fit. Here, the Gaussian was fully fitted at low energies (up to 2.1 eV) and partially at high energies. From the fitted Gaussian, the first absorption peak position and FWHM were extracted. Similarly, the PL data was smoothed (Savitzky–Golay) and fitted with a Gaussian. Due to the asymmetry of the PL, the Gaussian was fully fitted at high energies (up to 3.1 eV nm) and partially at low energies. This allowed for a better determination of the peak position. From the fitted Gaussian the PL peak position was extracted. The Stokes shift data were calculated by subtracting the PL peak position from the absorption peak position as determined from the fitted Gaussians. An example of a fitted absorption and PL spectra is shown in **Supplementary Fig. 6.** To convert to absorption bandgap of the $CsPbBr_3$ QDs into the QD size, we used the sizing curve published by Krieg *et al*[2]. Here, the model was fitted with an exponential fit (Belehradek, which gave the best fit), as shown in **Supplementary Fig. 7.**

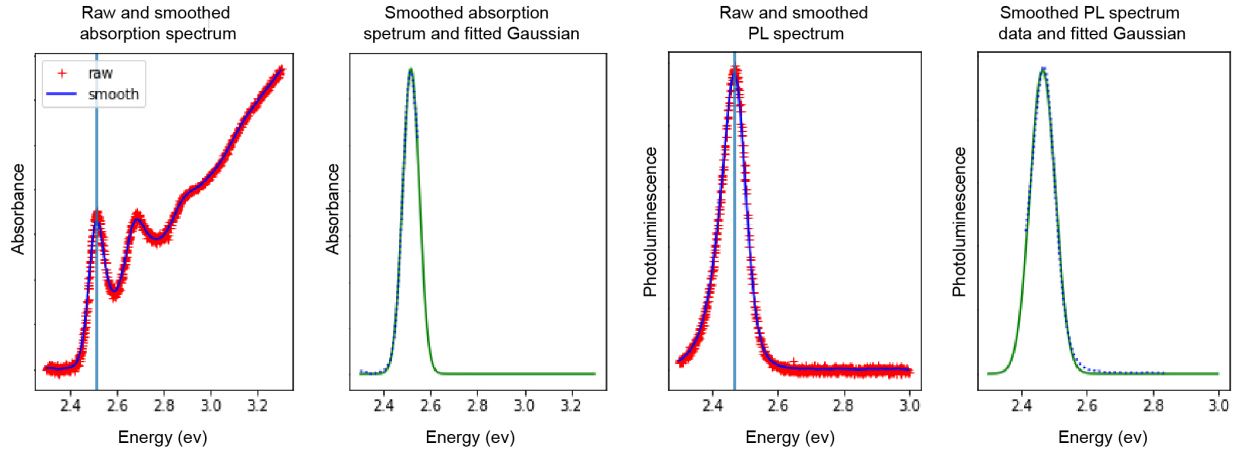

Supplementary Fig. 6 | Example of Gaussian fitting of absorption and PL data.

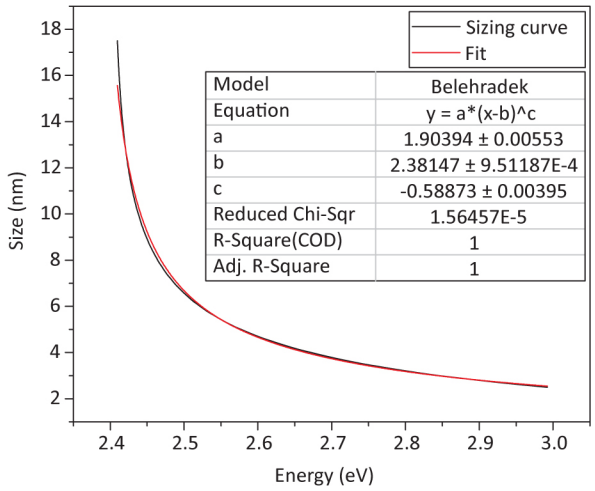

Supplementary Fig. 7 | Sizing curve used to convert the bandgap value into the QD size.

The higher order absorption peaks, as shown in **Figure 5,** were extracted from the negative second derivative of the absorption spectra. Here, absorption spectra were smoothed (Savitzky–Golay), followed by the calculation of the second derivative. The second derivative was further smoothed and a peak_find function was used to determine the final absorption peak positions. This process is shown in **Supplementary Fig. 8.** To confirm the error of the extracted properties, we performed an *in-situ* measurement with the same acquisition time as a growth time but with a pre-synthesized, purified sample. As shown in **Supplementary Fig. 9**, the standard deviation of the extracted absorption and PL peak positions is extremely low (0.02-0.04%, n = 1800). This error translates into a standard deviation of about 2% for the Stokes shift. As with the fitting of the bandgap, the extracted higher order peak positions have a standard deviation on the order of 0.001-0.4%.

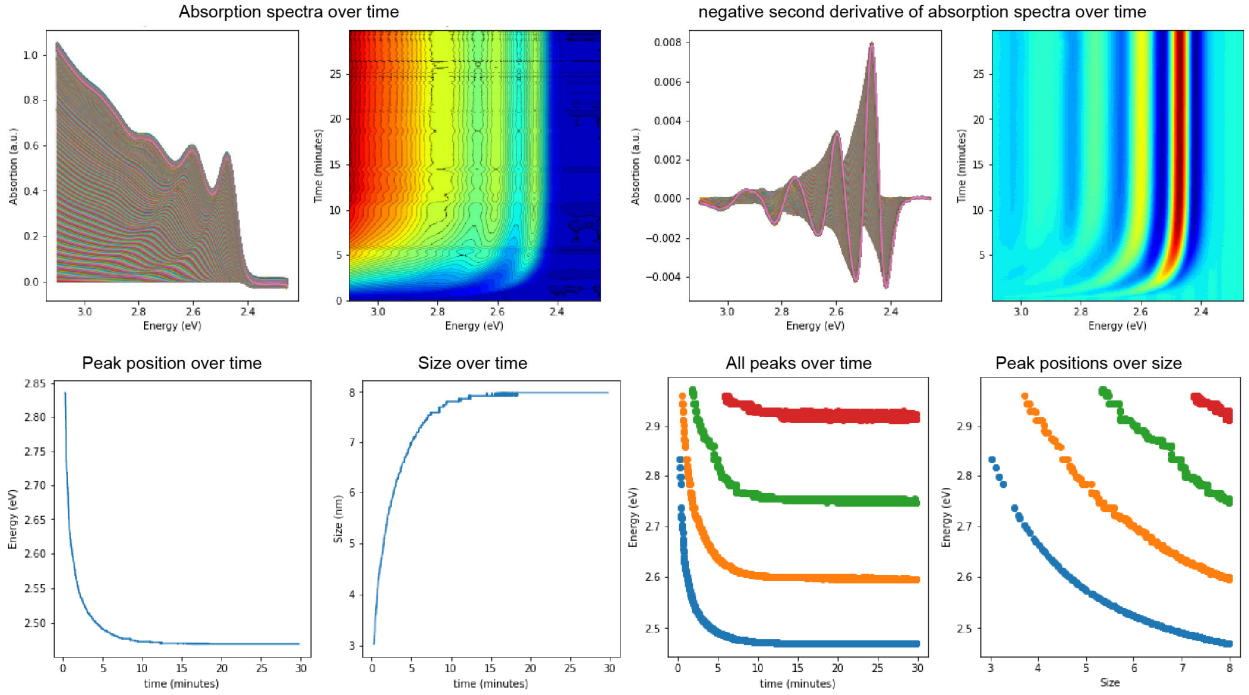

Supplementary Fig. 8 | Example of higher-order excitonic peak finding using second derivative.

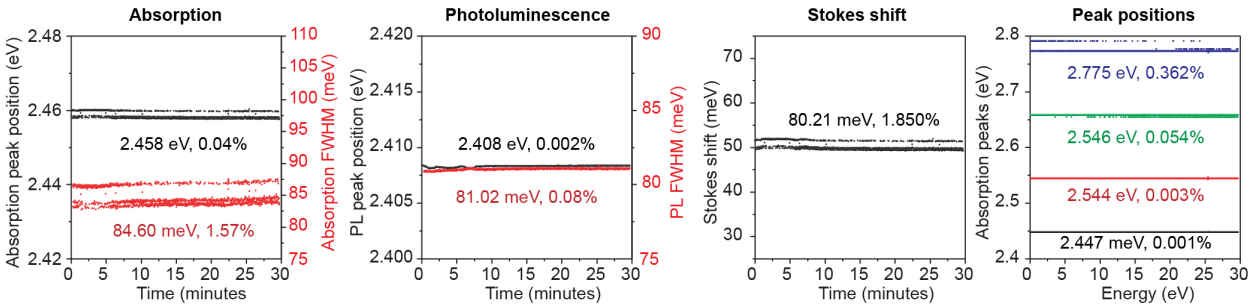

Supplementary Fig. 9 | Standard deviations of data extraction.

Supplementary Note 2: Calculations of the absorption spectra of perovskite QDs

Let M_{eh} be the reduced amplitude of the electron-photon matrix element[3]. The one-photon absorption cross-section at energy E can be evaluated by summing over all allowed transitions as follows

$$\sigma^{(1)}(E) = \frac{4\pi^2}{3} \frac{f_\varepsilon^2}{\sqrt{\varepsilon_{out}}\, c_0} \sum_{eh} \frac{1}{E_{eh}} |M_{eh}|^2 \; g_{eh}(E - E_{eh}) \,. \tag{S1}$$

In the above expression, c_0 is the speed of light in vacuum and $\frac{f_\varepsilon^2}{\sqrt{\varepsilon_{out}}}$ is the dielectric screening factor, which is taken to be the same for a cube and a sphere in the current calculation with $f_\varepsilon = \frac{3\varepsilon_{out}}{\varepsilon_{in} + 2\,\varepsilon_{out}}$. The value of ε_{in} is assumed to be the optical dielectric constant, which can be quite different from the effective dielectric constant ε_{eff} used for the Coulomb interaction. Each transition is broadened by a normalized line-shape function $g_{eh}(E - E_{eh})$, for which a further discussion can be found in **Supplementary Note 4**.

2.1 Effective Mass Approximation (EMA)

To compare absorption spectra of the spheroidal and cuboidal QDs, the EMA was used in which the envelope part of the total wave function is decoupled from the Bloch degree of freedom. Under the separation of length scales, the Bloch part, which varies on the atomic scale, can be integrated out leaving only the expressions for the envelope functions to be dealt with. The theoretical details for the cubic QD, to which the spherical case is similar, can be found below.

In the cubic confining potential that is given as

$$V_{\text{conf}}^{\text{cube}}(\vec{r}) = \begin{cases} 0, \text{ if } |i| < \dfrac{L_i}{2} \text{ for any } i = x, y, z, \\ \infty, \quad \text{otherwise,} \end{cases} \tag{S2}$$

the noninteracting single-particle wave function of the envelope part is

$$\psi_{n_x n_y n_z}^{\text{cube}}(\vec{r}) = \sqrt{\frac{8}{L_x L_y L_z}} \cos\left(\pi n_x \frac{x}{L_x} - \phi_{n_x}\right) \cos\left(\pi n_y \frac{y}{L_y} - \phi_{n_y}\right) \cos\left(\pi n_z \frac{z}{L_z} - \phi_{n_z}\right). \tag{S3}$$

The quantum numbers n_x, n_y, n_z are positive integers and their phase factors are defined as $\phi_{n_i} = \frac{\pi}{2}\, mod(n_i + 1{,}2), i = x, y, z$. The corresponding single-particle energy of the state in Eq. $(S3)$ is

$$E_{\text{conf}}^{\text{cube}}(n_x, n_y, n_z) = \frac{\hbar^2\pi^2}{2m^*}\frac{1}{L^2}\left(\frac{n_x^2}{b_x^2} + \frac{n_y^2}{b_y^2} + n_z^2\right). \quad (S4)$$

We note that the solution above is for a more general case where the QD shape is a rectangle cuboid of which the confining potential $V_{\text{conf}}^{\text{cube}}(\vec{r})$ is given as in Eq. $(S2)$. The ratios $b_x = L_x/L$ and $b_y = L_y/L$ (with $L_z = L$) describe the degree of shape anisotropy of the cuboidal QD. The three-tuple of quantum numbers (n_x, n_y, n_z) provides information on the symmetry of the state. In particular, the cubic state $(n_x, n_y, n_z) = (1,1,1)$ is equivalent to the spherical $1s$ state. Similarly, $(n_x, n_y, n_z) = (2,1,1)$, $(1,2,1)$ and $(1,1,2)$ correspond to $1p_x, 1p_y$ and $1p_z$, respectively. In the isotropic case, i.e. $b_x = b_y = 1$, the three $1p$ states are exactly degenerate, resulting in the same degeneracy equal to three as for the spherical $1p$ states. The relative energy difference between a sphere and an isotropic cube is around a few percent at most. For each optical transition allowed to the single exciton state $|eh\rangle = \psi_{n_x n_y n_z}^{\text{cube}}(\vec{r}_e)\, \psi_{n_x' n_y' n_z'}^{\text{cube}}(\vec{r}_h)\, a_c^\dagger a_v\, |\emptyset\rangle$ ($a^\dagger/a$ stands for the fermion creation/annihilation operator and $|\emptyset\rangle$ denotes the semiconductor ground state), the Coulomb interaction was computed using the single-particle wave function, Eq. $(S3)$,

$$E_{\text{Coul}}^{\text{cube}}(n_x, n_y, n_z;\, n_x', n_y', n_z') = \iint \psi^{*\text{cube}}_{n_x' n_y' n_z'}(\vec{r}_h)\, \psi^{*\text{cube}}_{n_x n_y n_z}(\vec{r}_e)\, V(\vec{r}_e, \vec{r}_h)\, \psi^{\text{cube}}_{n_x n_y n_z}(\vec{r}_e)\, \psi^{\text{cube}}_{n_x' n_y' n_z'}(\vec{r}_h)\, d\vec{r}_e\, d\vec{r}_h\ . \quad (S5)$$

Given that ε_{eff} is the effective dielectric constant of the QD material, the long-range Coulomb interaction $V_{12} = V(\vec{r}_1, \vec{r}_2)$ can be written as

$$V(\vec{r}_1, \vec{r}_2) = \frac{1}{\varepsilon_{eff}\, |\vec{r}_1 - \vec{r}_2|}\ . \quad (S6)$$

For a material with electronic band gap E_{gap}, the energy E_{eh} of a single exciton confined in a cubic QD is, thus,

$$E_{eh}^{\text{cube}} = E_{\text{gap}} + E_{\text{conf}}^{\text{cube}}(n_x, n_y, n_z) + E_{\text{conf}}^{\text{cube}}(n_x', n_y', n_z') + E_{\text{Coul}}^{\text{cube}}(n_x, n_y, n_z;\, n_x', n_y', n_z'). \quad (S7)$$

The energy E_{eh}^{cube} contains the Coulomb interaction from a single-shot computation without self-consistency iteration and wave function relaxation. The single-shot computation of $E_{\text{Coul}}^{\text{cube}}$ seems to suffice for the current purpose of comparing the cubic and spherical absorption spectra.

The final input to the expression for the single-photon absorption cross-section $\sigma^{(1)}$ is the transition amplitude M_{eh}, which take the following simple expression in the EMA,

$$|M_{eh}|^2 = E_P\, \delta_{n_x^e n_x^h}\, \delta_{n_y^e n_y^h}\, \delta_{n_z^e n_z^h}. \quad (S8)$$

The Kane parameter E_P is directly related to the optical matrix element between the lowest conduction and highest valence bands. Before being broadened with a line-shape function to obtain $\sigma^{(1)}$, the expression $\Xi_{eh} = \frac{4\pi^2}{3}\frac{f_\varepsilon^2}{\sqrt{\varepsilon_{out}}\, c_0}\frac{1}{E_{eh}}|M_{eh}|^2$ is sometimes referred to as the oscillator strength for the transition from the ground state $|\emptyset\rangle$ to the exciton state $|eh\rangle$.

The spherical calculations used the same method and numerical code as outlined in reference 3.~~Error! Reference source not found..2~~. At this level of theory, the conduction-valence band coupling was turned off by setting the Kane parameter to 0 in the $k.p$ Hamiltonian. As a useful remark, the spherical transition amplitude M_{eh} satisfies

$$|M_{eh}|^2 = E_P\, \delta_{l_e l_h}\, \delta_{m_e m_h} \delta_{n_e n_h}, \quad (S9)$$

where n_e and n_h are the principal quantum numbers of the electron and hole states. The above selection rule implies that the only optically allowed transitions in EMA are $1s-1s, 1p-1p, 1d-1d$, etc. named according the various spherical angular momenta and principal quantum numbers. Strictly speaking, this is no longer true for the $k.p$ model even though these transitions remain the ones giving major contributions.

To make a fair comparison between a cube and a sphere, we used the following relation between the sphere radius R and the cube edge length L where

$$L = \sqrt{3}\, R. \tag{S10}$$

Relation $(S10)$ was chosen such that the lowest noninteracting single-particle energies (i.e. of the $1s$ state) of an isotropic cuboid and the equivalent sphere are identical. In fact, this relation leads to the entire s-series energies to coincide for both geometries, see formulae **Error! Reference source not found.** $(S4)$ and **Error! Reference source not found.** $(S11)$.

$$E_{\text{conf}}^{\text{sph}}(n, l = 0) = \frac{\hbar^2 \pi^2}{2m^*} \frac{n^2}{R^2}\ . \tag{S11}$$

Besides, it turns out that the computed Coulomb interacting energies, without self-consistency, for the $1s$ come out to be very similar to the one of a cube, having a relative difference of around a few percent from one another. Thus, the relation **Error! Reference source not found.** $(S10)$ is justified for the comparative study between the spherical and cubic absorption spectra. Using this relation between L and R, one can arrive at the conclusion that the excitonic features are more pronounced in a sphere than its equivalent cube, as discussed in the main text.

2.2. Two-band $k.p$ model and Hartree-Fock approximation

Due to large spin-orbit splitting in lead halide perovskites, the band edges at the R-point of the Brillouin zone consist of an s-like conduction and a $p_{1/2}$-like valence band with R_6^- and R_6^+ symmetries respectively. (s and p refer to the orbital angular momenta of the Bloch functions). Therefore, the two-band $k.p$ model (also known as $4 \times 4\ k.p$ model) is well-suited to describe the dispersion of electrons and holes around the R-point. In particular, we considered here the spherically symmetric $k.p$ Hamiltonian $H_{k.p}$. In a spherical confinement V_{ext}, the total angular momentum $\vec{F} = \vec{l} + \vec{J}$ is a conserved quantity, where $\vec{l}$ is the orbital angular momentum of the envelope function and $\vec{J}$ is the angular momentum of the Bloch part. In other words, an eigenstate of $H_{k.p}$ in the external potential V_{ext} can be written as

$$|\eta F m_F\rangle = \frac{\mathcal{R}_s(r)}{r} \left| \left(l, \frac{1}{2}\right) F m_F \right\rangle + \frac{\bar{\mathcal{R}}_p(r)}{r} \left| \left(\bar{l}, \frac{1}{2}\right) F m_F \right\rangle, \tag{S12}$$

where $\mathcal{R}_s(r)$ and $\bar{\mathcal{R}}_p(r)$ are the radial components of the envelope wave functions corresponding to the s-like and $p_{1/2}$-like bands, respectively[4].

At mean-field level, the Coulomb interaction between the charge carriers can be approximated using the Hartree-Fock (HF) potential. The HF equation for an occupied state $|a\rangle$ (i.e. a state with a charge present) is defined to be

$$\left(H_{k.p} + V_{\text{conf}}^{\text{sph}} + V_{HF}^{av}\right) |a\rangle = \epsilon_a |a\rangle. \tag{S13}$$

The first two terms give rise to the confined kinetic energy of a carrier trapped inside the QD. The third term $V_{HF}^{av} = V_{dir} + V_{exc}$ is the spherically averaged HF potential, which is the sum of the direct and exchange interaction over all occupied electron and hole states $|b\rangle$. Explicitly,

$$\begin{aligned} \langle i|V_{dir}|a\rangle &= \sum_b^{occ} e_b q_b^a \langle ib|V_{12}|ab\rangle\,, \\ \langle i|V_{exc}|a\rangle &= -\sum_b^{occ} e_b q_b^a \langle ib|V_{12}|ba\rangle\,, \end{aligned} \tag{S14}$$

where $|a\rangle, |b\rangle, \ldots$ denote the occupied states and $|i\rangle$ is any arbitrary state (occupied and unoccupied). We followed the charge convention $e_b = 1$ and -1 for electron and hole, respectively[4]. The weight q_b^a represents

the averaged occupation of a shell B, containing the state $|b\rangle$, relative to the state $|a\rangle$ in shell A. Additional details of the $k.p$ model and the HF formalism can be found in reference 4. We briefly note that the current formalism can be used to describe, at the HF (mean-field) level, systems of N_e electrons and N_h holes, subsuming the case of a single exciton but not only. Letting q_a be the fractional occupation of shell A, the HF energy of the aforementioned system is

$$E_{HF}^{av} = \sum_{a}^{occ} e_a q_a \left\langle a\middle|H_{k.p} + V_{\text{conf}}^{\text{sph}}|a\right\rangle + \frac{1}{2}\sum_{a}^{occ} e_a q_a \left\langle a|V_{HF}^{av}|a\right\rangle . \qquad (S15)$$

The HF energy is useful for estimating the energy needed to add or remove a particle (electron or hole) from the system, which can be regarded as the Koopmans' theorem for the envelope degree of freedom.

Most importantly, the HF potential can be used to generate a complete basis set, called the HF basis set, that can be used, for instance, in the many-body calculations for the electron-photon interaction and other correlation corrections[3,4]. Here, we only summarize the important conclusions while the details of second-order many-body perturbation theory for one-photon absorption can be found in reference 3. The interband electron-photon matrix elements receive a significant correction from correlation effects. An enhancement of the lower excitonic transitions has been demonstrated to improve the shape of the absorption curve. Notably, the lowest $1s-1s$ exciton receives a large correction factor, which is directly linked to the sub-nanosecond radiative lifetime at cryogenic temperature[4]. For these reasons, the second-order many-body perturbation theory was employed for the calculation of the cross-section $\sigma^{(1)}$ as shown in Figure 4g in the main text.

Finally, we discuss the parameters used in these empirical methods. The fundamental input parameters that are the reduced effective mass $\mu = 0.126$ and effective dielectric constant $\varepsilon_{eff} = 7.3$ are taken from Yang *et al*[5]. for $CsPbBr_3$. The electron and hole effective masses were assumed to be equal leading to $m_e^* = m_h^* = 2\mu$. From the deduced m_e^* and m_h^*, the input $m^* = m'$ in Eq. **~~Error! Reference source not found.~~** $(S4)$ and Eq. **~~Error! Reference source not found.~~** $(S11)$ is obtained from applying the formula for the energy-dependent effective mass m' in reference 6. The electronic band gap is set to be $E_{\text{gap}} = 2.424$ eV, which is consistent with the value used in Krieg *et al*[2]. For $FAPbBr_3$ and $MAPbBr_3$, the reduced effective mass μ and effective dielectric constant ε_{eff} are taken from Galkowski *et al*[6]. The value for the Kane parameter E_P was chosen to be $E_P = 20.0$ eV for all three A-site cations[4]. Note that this conservative value lies in between the various estimates coming from the two-band and four-band $k.p$ models. Again, additional information is required to correctly assess the actual value of E_P, which we leave for future work. The EMA in spherical geometry can be obtained by switching off the conduction-valence band coupling (i.e. setting $E_P = 0$) in the $k.p$ Hamiltonian while keeping the optical matrix element, which is proportional to $\sqrt{E_P}$, nonzero.

Supplementary Note 3: Additional mechanistic studies.

To accurately calculate the concentration of the $PbBr_2$ and $PbBr_3^-$ precursors during the growth, we firstly determined their respective molar absorption coefficient as shown in **Supplementary Fig. 10.** Here, the molar absorption coefficient of the $PbBr_2$[TOPO] complex was determined by measuring the optical density at 4.4 eV of solutions with different concentration of $PbBr_2$[TOPO] in hexane. For the molar absorption coefficient of $PbBr_3^-$, a small excess of didodecyldimethylammonium bromide (DDAB, 98%, purchased from Sigma Aldrich) dissolved in chloroform ($CHCl_3$, 99.8%, purchased from Sigma Aldrich) was added to the $PbBr_2$[TOPO] solutions. This resulted in the $PbBr_3^-$ absorption band appearing at 3.85 eV, matching that of the one measured for the Cs[$PbBr_3$] complex.

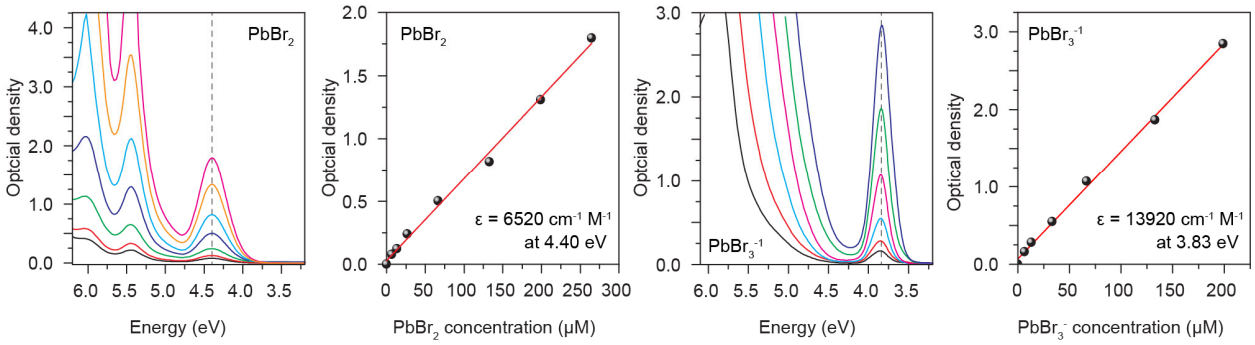

Supplementary Fig. 10 | Determination of molar extension coefficients of $PbBr_2$ and Cs[$PbBr_3$]TOPO complexes in hexane.

To determine the $PbBr_2$, $PbBr_3^-$, $CsPbBr_3$ and $PbDOPA_2$ concentration *in-situ*, we firstly determined the concentration of $CsPbBr_3$ at 3.1 eV, based on the reported extinction coefficient by De Roo *et al*[7]. Due to the absorption onset of the growing $CsPbBr_3$ QDs, we subtracted an absorption spectrum of large washed $CsPbBr_3$ QDs scaled to the absorption at 3.1 eV; this process is shown in **Supplementary Fig. 11**. This allowed us to determine the concentration of $PbBr_2$, $PbBr_3^-$, without the absorption onset of $CsPbBr_3$. The remaining absorption spectra were fitted with Gaussians fixed at 4.4 and 3.83 eV. The resulting peak maxima of these fits were used as OD and to directly calculate the respective $PbBr_2$ and $PbBr_3^-$ concentrations. Based on the proposed reaction mechanism as shown in **Figure 3**, we calculated the $PbDOPA_2$ concentration by extracting the $PbBr_2$, $PbBr_3^-$, $CsPbBr_3$ concentrations from the starting $PbBr_2$ quantity.

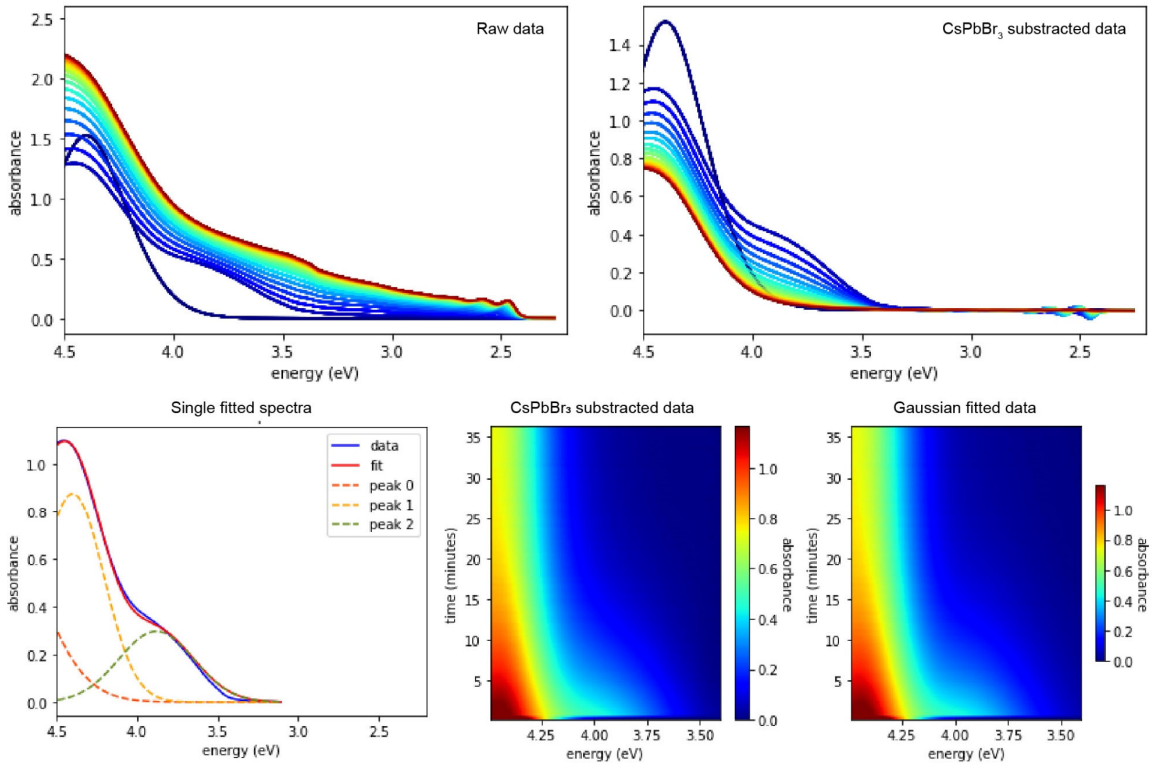

Supplementary Fig. 11 | Example of fitting and extraction of $PbBr_2$ and $PbBr_3^-$ concentrations.

We further confirm the $PbBr_2$:Cs[$PbBr_3$] equilibrium by shifting it towards the Cs[$PbBr_3$] side. This can be done by replacing Cs-DOPA with Cs-oleate solution with an excess of free oleic acid. As demonstrated by Almeida *et al*[8]., free oleic acid is strong enough to protonate TOPO and form $PbBr_3^-$ (most likely in the form of $PbBr_3$:TOPOH). As shown in **Supplementary Fig. 12,** replacing Cs-DOPA with Cs-OA results in the fast growth of polydisperse $CsPbBr_3$ QDs. This can be explained by the fact that the excess free OA in the Cs-OA precursor immediately and fully shifts the $PbBr_2$/$PbBr_3^-$ equilibrium to the $PbBr_3^-$ side, making it fully available for the nucleation. Thus, there exists no inherent mechanism for retaining some precursor for the growth stage. This is analogous to the conventional $CsPbBr_3$ nanocrystal synthesis[9], wherein there exists no temporal separation of the nucleation and growth, and the nanocrystal size is usually controlled by the synthesis temperature.

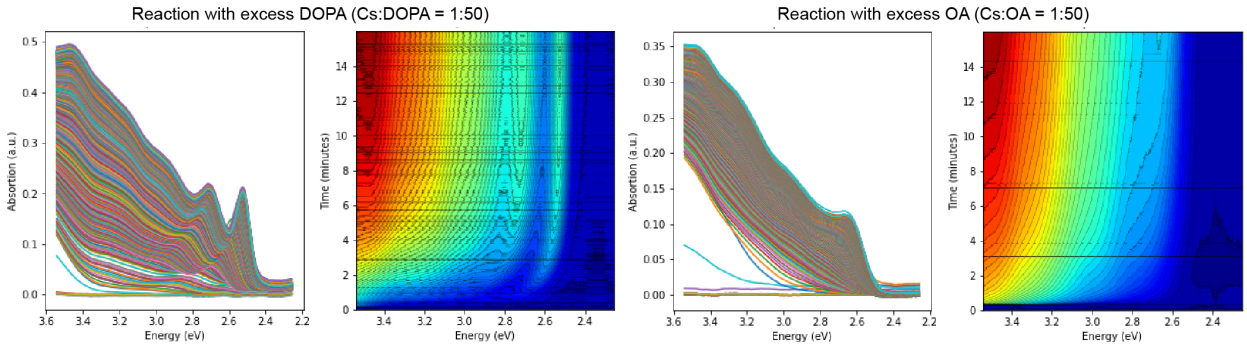

Supplementary Fig. 12 | Comparison of Cs-DOPA vs Cs-OA. Here, the free OA results in the immediate formation of $PbBr_3^-$, vastly accelerating the reaction, as is apparent from the initial increase in OD at the start of the reaction. The fast reaction in this case also leads to the formation of more polydisperse QDs, seen as poorly resolved absorption features.

Supplementary Note 4: **Modelling of the broadening mechanisms**

In the formula **Error! Reference source not found.** $(S1)$ used for calculating the absorption cross-section, the line shape g_{eh} was assumed to have the Voigt profile

$$g_{eh}(x) = V(x, \sigma, \Gamma) = \int_{-\infty}^{\infty} G(x', \sigma)\, L(x - x', \Gamma)\, dx' , \qquad (S16)$$

which is a convolution between the normalized Gaussian $G(x, \sigma) = \frac{1}{\sqrt{2\pi}\,\sigma} \exp(-\frac{x^2}{2\sigma^2})$ and Lorentzian $L(x, \Gamma) = \frac{1}{\pi} \frac{\Gamma}{x^2 + \Gamma^2}$ distributions. The total width of the above Voigt function can be approximated with an error less than 0.02% as

$$\mathrm{f}_V = \frac{C_1}{2}\, \mathrm{f}_{\Gamma} + \sqrt{\left(\frac{C_2}{2}\right)^2 \mathrm{f}_{\Gamma}^2 + \mathrm{f}_{\sigma}^2} , \qquad (S17)$$

where $C_1 = 1 + 0.099 \ln(2)$ and $C_2 = (1 - 0.099 \ln(2))^2$.[10] Here, f_σ is the full-width at half-maximum (FWHM) of the Gaussian such that $\mathrm{f}_\sigma = 2\sqrt{2 \ln(2)}\, \sigma$ and the standard deviation σ was approximated from the standard deviation of the size variation $\delta_{size} = \delta L / \langle L \rangle$ by using the following Taylor series expansion.

$$\sigma = \sum_i \sigma^{(i)}\, (\delta_{size})^i , \qquad (S18)$$

where $\sigma^{(i)} = (-1)^i\, [(i+1) E_{\mathrm{conf}} + E_{\mathrm{Coul}}]$, E_{conf} and E_{Coul} are the confined kinetic energy and Coulomb interaction energy, respectively. Note that, roughly speaking, $E_{\mathrm{conf}} \propto L^{-2}$ whereas $E_{\mathrm{Coul}} \propto L^{-1}$ and $\sigma^{(i)}$ comes from the derivative of the exciton energy $E = E_{\mathrm{gap}} + E_{\mathrm{conf}} + E_{\mathrm{Coul}}$ with respect to L. Summing up to the fifth order derivative shows sufficient convergence of the Taylor expansion. The Gaussian distribution of width σ represents the static inhomogeneous broadening due to the random distribution of the QD sizes, which is practically independent of temperature T.

Apart from σ, there is also some T-dependent contribution to the line width that, in our current work, was modelled under the assumption that all transitions receive the same amount of homogeneous broadening. The largest contribution to this homogeneous broadening coming from the interaction with longitudinal-optical (LO) phonons was supposed to involve only a single effective phonon mode E_{LO}. Additionally, the T-dependent FWHM f_Γ for the Lorentzian function can be written as

$$\mathrm{f}_\Gamma = 2\Gamma = 2\, (\Gamma_0 + \sigma_{Ac} T + \Gamma_{LO}\, N_{LO}). \qquad (S19)$$

The first term Γ_0 is the spectral diffusion that characterizes the amount of broadening at $T = 0\ K$. The second expression, which is linear in T, describes the interaction with acoustic phonons. Γ_{LO} is the electron-LO phonon coupling rate assuming the perturbative interaction where the total rate is proportional to the phonon occupation number $N_{LO} = \frac{1}{\exp\left(\frac{E_{LO}}{k_B T}\right) - 1}$, which follows the Bose-Einstein statistics.

The measured Γ_0 from single-dot spectroscopy shows $\Gamma_0 = 0.4$ meV for $CsPbBr_3$[11]. For our current purpose, we shall let $\Gamma_0 = 0$ without any alteration of the basic conclusions. Taking the experimental values $\sigma_{Ac} = 8{\times}10^{-3}$ meV$/K$ and $E_{LO} = 16$ meV11, we obtained the fitted value of $\Gamma_{LO} = 22$ meV from our experimental data by using nonlinear curve-fitting "*lsqcurvefit"* in GNU Octave. This value of Γ_{LO} from the absorption data is smaller than the value $\Gamma_{LO} = 42$ meV that was deduced from single-dot PL measurements by Ramade *et al*[Error! Reference source not found.12]. These diverse values of the Γ_{LO} coupling coefficient reflects the difference in the nature of electron-phonon coupling between absorption and PL processes. Most likely, a better description of the homogeneous broadening should also involve multiple LO phonon modes.

Besides the formula **Error! Reference source not found.** $(S19)$ including only one effective LO phonon mode at $E_{LO} = 16$ meV albeit retaining the underlying physical mechanism, we note that the experimental data were better fitted using a pure Gaussian function than a Gaussian-Lorentzian convolution. This observation seems to indicate the fact that the electron-phonon interaction potentially

acquires some degree of statistical randomness due to, for instance, the dependence of the phonon spectrum on the QD size L and the distribution of L. The size-dependent estimation of σ based on the size variation δ_{size} reproduces excellently the width of the first absorption peak (at low T) while somewhat overestimate σ for higher transitions. Thus, the mechanism for inhomogeneous broadening may also need to be revisited. As a conclusion, additional experimental and theoretical investigations are required to unveil the fundamental features of the electron-phonon coupling as well as of the broadening mechanism of the absorption peaks.

Supplementary Note 5: **Splitting among the 1p-1p states**

The experimental absorption spectra at 14 K exhibit two distinct peaks for the 1p-1p transitions where the lower-energy peak has twice the integrated area of the one at higher energy. In this Supplementary Note, we base our discussion around the splitting among 1p-1p states on mass and shape anisotropy. We note that the latter has been discussed in Krieg *et al*[2]. As shown below, ~~the while~~ while the contributions from these two anisotropic sources are non-negligible, the mass anisotropy may provide an even more significant effect compared to the shape anisotropy.

Ab initio calculations based on the orthorhombic structure result in slightly different masses along the various crystallographic axes[12,13]. Among them, the masses along two directions, labelled as $\hat{e}_1$ and $\hat{e}_2$, are very similar (or the same in some calculations) and slightly bigger than the mass m_{33} along the third axis $\hat{e}_3$. We defined the average effective mass $\langle m \rangle$ as follows.

$$\frac{1}{m_{11}} + \frac{1}{m_{22}} + \frac{1}{m_{33}} = \frac{1}{\langle m \rangle} \tag{S20}$$

From the expression **~~Error! Reference source not found.~~** $(S20)$, the dimensionless mass variations are defined as

$$\left(\frac{\delta m}{m}\right)_{11} = \left(\frac{\delta m}{m}\right)_{22} = -\frac{1}{2}\frac{\delta m}{m}, \left(\frac{\delta m}{m}\right)_{33} = \frac{\delta m}{m}, \tag{S21}$$

where the masses along the $\hat{e}_1$ and $\hat{e}_2$ axes have been taken to be equal, i.e. $m_{11} = m_{22}$.

The effect of different masses along the three axes can be treated by considering the corresponding change in kinetic energy as a perturbation, leading to the following Hamiltonian:

$$H_{\delta m} = \begin{pmatrix} \left(\frac{\delta m}{m}\right)_{11} \frac{k_1^2}{\langle m \rangle} & 0 & 0 \\ 0 & \left(\frac{\delta m}{m}\right)_{22} \frac{k_2^2}{\langle m \rangle} & 0 \\ 0 & 0 & \left(\frac{\delta m}{m}\right)_{33} \frac{k_3^2}{\langle m \rangle} \end{pmatrix}. \tag{S22}$$

Note that $\frac{k_i^2}{\langle m \rangle}$ in Eq. **~~Error! Reference source not found.~~** $(S22)$ gives the kinetic energy of the 1p state along direction $\hat{e}_i$ when applied on the corresponding wave function. This renders the calculations of 1p-1p splitting due to the mass variation semi-analytical. We chose to work in the EMA with cubic confining potential as discussed in **Supplementary Note 2.1** to also incorporate the anisotropic shape that is described by the aspect ratio below.

$$b_x = b_y = b > 1 \tag{S23}$$

The condition in **~~Error! Reference source not found.~~** $(S23)$ is equivalent to L_x and L_y being equal to each other and bigger than L_z, which implies that the p_z state with quantum number $(n_x, n_y, n_z) = (1,1,2)$ is higher in energy compared to the $p_{x/y}$ state with $(n_x, n_y, n_z) = (2,1,1)$.

Let $\Delta E_{1p}^{\delta m/m}$ and ΔE_{1p}^{b} be the amount of splitting coming from the mass and shape anisotropy respectively. Briefly speaking, $\Delta E_{1p}^{\delta m/m}$ is the difference in the energies of the wave functions along $\hat{e}_{1/2}$ and $\hat{e}_3$ whereas $\Delta E_{1p}^{b} = E_{\text{conf}}^{\text{cube}}(1,1,2) - E_{\text{conf}}^{\text{cube}}(2,1,1)$ is the difference in the confined kinetic energies along L_x and L_z. The upper and lower bounds for the 1p-1p splitting can be obtained by looking at the relative orientation between the crystallographic axes and the edges of a QD. When $\hat{e}_3$ is aligned along L_z, the total splitting amongst the 1p-1p transitions is

$$\Delta E_{1p}^{U} = \Delta E_{1p}^{\delta m/m} + \Delta E_{1p}^{b}. \quad (S24)$$

If instead $\hat{e}_3$ is perpendicular to L_z, the splitting is given as the difference between the two contributions $\Delta E_{1p}^{\delta m/m}$ and ΔE_{1p}^{b}, i.e.

$$\Delta E_{1p}^{L} = \left|\Delta E_{1p}^{\delta m/m} - \Delta E_{1p}^{b}\right|. \quad (S25)$$

Eq. **~~Error! Reference source not found.~~** $(S24)$ provides an upper limit ΔE_{1p}^{U} for the splitting involving anisotropic mass and shape while ΔE_{1p}^{L} in Eq. **~~Error! Reference source not found.~~** $(S25)$ marks the associated lower limit. From the results of the current calculations in **Supplementary Fig. 29**, $\Delta E_{1p}^{\delta m/m}$ is larger than ΔE_{1p}^{b}, which indicates the importance of the mass variation along the various crystal axes, an aspect that has not received much consideration in the literature so far. The parameter choice leading to this observation will be discussed next.

Our SAXS measurements suggest an aspect ratio roughly $b = 1.03$. Ab initio calculations by Traoré *et al*[12]. imply a level of mass variation of about $\delta m/m = 10\%$ from various DFT flavors using the room temperature crystal structure for $CsPbBr_3$. The values of $\Delta E_{1p}^{\delta m/m}, \Delta E_{1p}^{b}, \Delta E_{1p}^{L}$ and ΔE_{1p}^{U} versus the 1s-1s exciton energy $E_{1s\text{-}1s}$ obtained with this choice of $\delta m/m$ and various aspect ratios $b = 1.03, 1{,}05$ and 1.10 are given in **Supplementary Fig. 29**. Here, we note that the measured value of the aspect ratio alone, which describes the p-state splitting due to the QD shape, cannot reproduce the right order of magnitude of the experimental splitting even by using $b = 1.10$, which is certainly exaggerated compared to the measured SAXS data. The proposed mechanism of mass anisotropy with $\delta m/m = 10\%$, however, is able to bring ΔE_{1p} to a good agreement with the measured data even with much smaller shape anisotropy $b = 1.03$, especially considered within the experimental uncertainty from low-T absorption and PLE experiments. Additional calculations with other values of the mass variation $\delta m/m$ (while keeping $b = 1.03$) can be found in **Extended Data Fig. 8.** of the main text. These results suggest that the p-state splitting is intrinsic, which may come from various anisotropic origins, other than being extrinsic due to the shape of the QDs. In what follows, we speculate potential sources of anisotropy in these perovskite QDs.

Numerous experiments via XRD techniques shows that, for temperature less than 300 K, $CsPbBr_3$ in orthorhombic phase has two roughly equal lattice parameters that are different from the third, to which the theoretical approach conforms[14-16]. As the temperature keeps rising beyond 300 K, the crystal structure makes a transition from orthorhombic to the more symmetric tetragonal and, subsequently, cubic phases[14,15,17]. The crystal structure and, as a consequence, the effective mass tensor become increasingly more isotropic, indicating more splitting at low temperature. Together with the broadened line shape at higher T, this conforms with the appearance of a single, well-defined 1p-1p peak at room-T spectra while observing some splitting at low temperature. Some supporting calculations are shown in **Supplementary Fig. 30**.

Recent studies imply that the transition temperature from orthorhombic to tetragonal and then cubic phases may be lowered in QDs of smaller sizes[18]. Besides, as the size decreases, the degree of lattice distortion and lead-halide octahedral tilting may also be affected. Small perovskite QDs of 5-10 nanometers have been shown to exhibit some cubic structure even at room temperature[19]. These experiments signify an observable dependence of the crystal lattice and the effective mass on the QDs size. Furthermore, it is worthwhile to mention that certain level of strain can also introduce changes in the effective mass of the nanostructures[20-22]. This strain-induced variation, which may be ligand-mediated or facet-specific, may possibly depend on the shape being cuboidal or spheroidal.

As a result, and in summary, we put forward the role of mass anisotropy in the splitting of the observed 1p-1p transitions in the optical spectra at low temperatures, which shall be further studied.

Supplementary Tables

Supplementary Table 1. Reactions from the Main Text.

$CsPbBr_3$						
Figure	**label**	**Amount of hexane (ml)**	**Amount of $PbBr_2$-TOPO stock solution (µl)**	**Amount of Cs/FA/MA stock solution (µl)**	**Amount of additional TOPO stock solution (µl)**	**Final size (nm)**
Fig 1c	-	6	80	40	160	6.2
Fig 1d	-	0-25	80	40	0	3.1-13
Fig 1e	-	6	2000	1000	0	6.2
Fig 1h/i	483 uM	6	320	160	320	8.2
Fig 1h/i	256 uM	6	160	80	160	6.1
Fig 1h/i	132 uM	6	80	40	80	4.4
Fig 1h/i	34 uM	6	40	20	40	3.4
Fig 1j/k	1:20	6	80	40	240	8.7
Fig 1j/k	1:15	6	80	40	160	6.2
Fig 1j/k	1:10	6	80	40	80	4.4
Fig 1j/k	1:5	6	80	40	0	3.5
Fig 1l*	Conventional	0	4000	75	-	6.3
Fig 1l	Dilution control	6	1280	160	160	7.2
Fig 1l	Dilution + TOPO control	6	40	20	160	7.3
Fig 3e	-	6	80	40	80	4.4
Fig 3f	See Figure 3c/d					
Fig 4b	-	6	160	80	320	8.0
$FAPbBr_3$ and $MAPbBr_3$						
Figure	**label**	**Amount of hexane (ml)**	**Amount of Pb-TOPO stock solution (µl)**	**Amount of CFA/MA stock solution (µl)**	**Amount of additional DOPA stock solution (µl)**	**Final size (nm)**
Fig 5a	-	6	100	100	100	~7
Fig 5b	6.0 nm	6	100	100	100	6.0
Fig 5b	6.8 nm	6	100	150	100	6.8
Fig 5b	8.8 nm	6	150	250	-	8.8
Fig 5b**	11 nm	6	150	250	-	11
Fig 5e**	-	24	200	200	100	~7
Fig 5f**	5.7 nm	400	800	24000	1000	5.7
Fig 5f**	7.0 nm	24	200	200	100	7.0
Fig 5f**	9.0 nm	400	400	24000	400	9.0
Fig 5f**	9.9 nm	150	250	6000	-	9.9
Fig 6a	$CsPbBr_3$	See Figure 1c				6.8
Fig 6a	$FAPbBr_3$	See Figure 5b				7.2
Fig 6a	$MAPbBr_3$	See Figure 5f				7.0

*Performed with 10 times higher DOPA concentration

** performed with cooling solutions in ice bath prior to injection

Supplementary Table 2: Reaction conditions from Supplementary Information.

$CsPbBr_3$						
Supplementary Figure	**label**	**Amount of hexane (ml)**	**Amount of $PbBr_2$-TOPO stock solution (µl)**	**Amount of Cs- stock solution (µl)**	**Amount of additional TOPO stock solution (µl)**	**Final size (nm)**
Fig 1	0.5 mM	6	80	40	320	4.4
Fig 1	1 mM	6	160	40	320	5.4
Fig 1	2 mM	6	320	40	320	7.0
Fig 2	1:2	4.2	800	800	-	7.0
Fig 2	1:320	10.4	1600	10	-	4.5
Fig 3	-	3	20	40	20	-
Fig 4	1:5	6	80	40	80	4.4
Fig 4*	1:75	6	80	40	80	4.6
Fig 5	-	5	800	50	-	4.2
Fig 18	See main text Fig. 1k					
Fig 26**	-	3	20	10	20	4.8
Fig 27	See main text Fig. 3f					

* The amount of DOPA in the Cs-DOPA precursor was increased by 15 times
** Performed on conventional absorption spectrometer

Supplementary Figures 13-33.

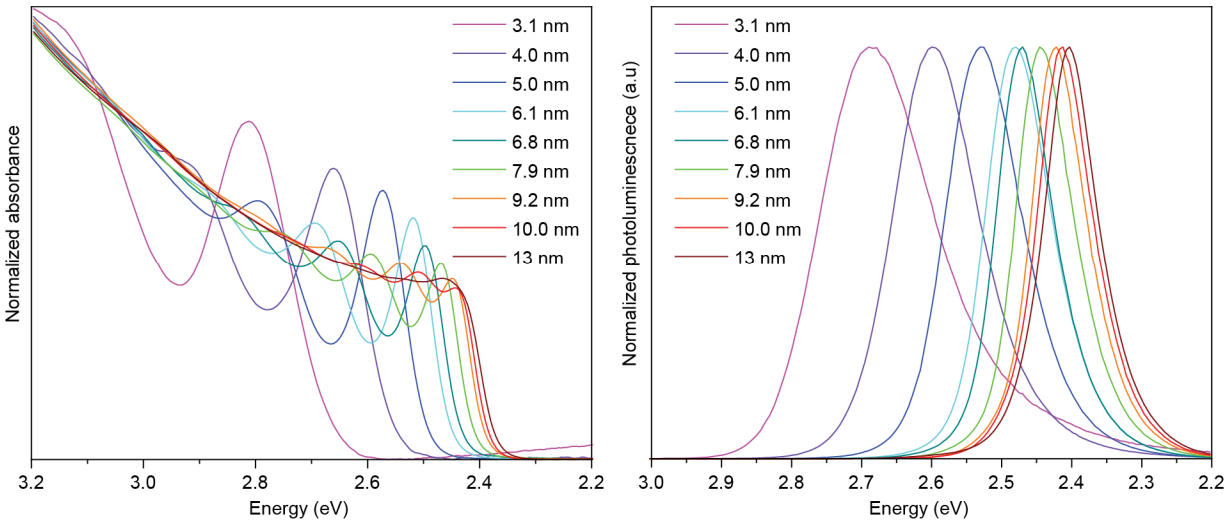

Supplementary Fig. 13 | Additional absorption and PL spectra of purified $CsPbBr_3$ QDs.

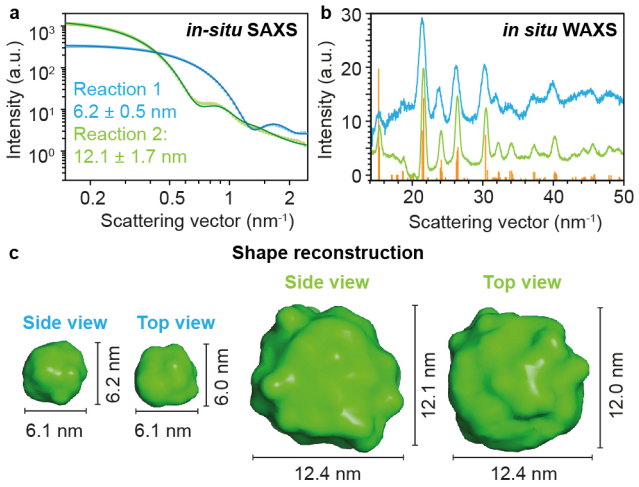

Supplementary Fig. 14 | Additional *in-situ* SAXS and WAXS measurements of 12 nm $CsPbBr_3$ QDs. **a,** Comparison of *in-situ* SAXS scattering curve and its fit for 12 and 6 nm $CsPbBr_3$ QDs. **b,** *In-situ* WAXS pattern of 12 and 6 nm $CsPbBr_3$ QD, both matching with the orthorhombic $CsPbBr_3$ crystal structure. **c,** Particle shape reconstruction[23] of 6 and 12 nm $CsPbBr_3$ QDs, both indicating a near isotropic spherical shape.

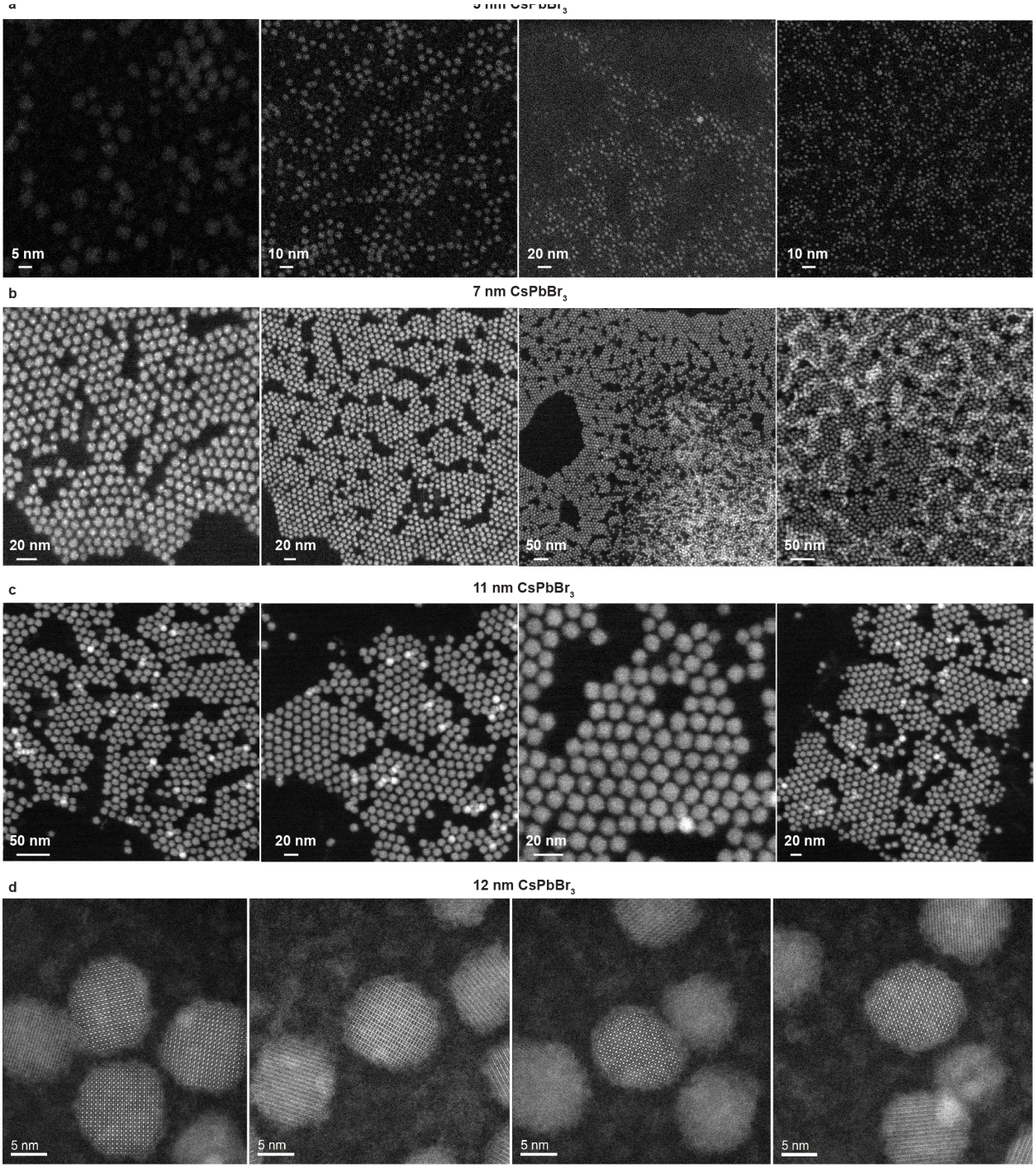

Supplementary Fig. 15 | Additional DF-TEM, HAADF-STEM and HR-HAADF-STEM images of spherical $CsPbBr_3$ QDs. a-c, HAADF-STEM images of different sized $CsPbBr_3$ QDs, with larger QDs clearly showing hexagonal assemblies, demonstrating their spheroidal shape. **d,** HR-HAADF-STEM images of large 12 nm $CsPbBr_3$ QDs, clearly demonstrating the spheroidal shape, as a result from truncating along the {110} and {111} facets.

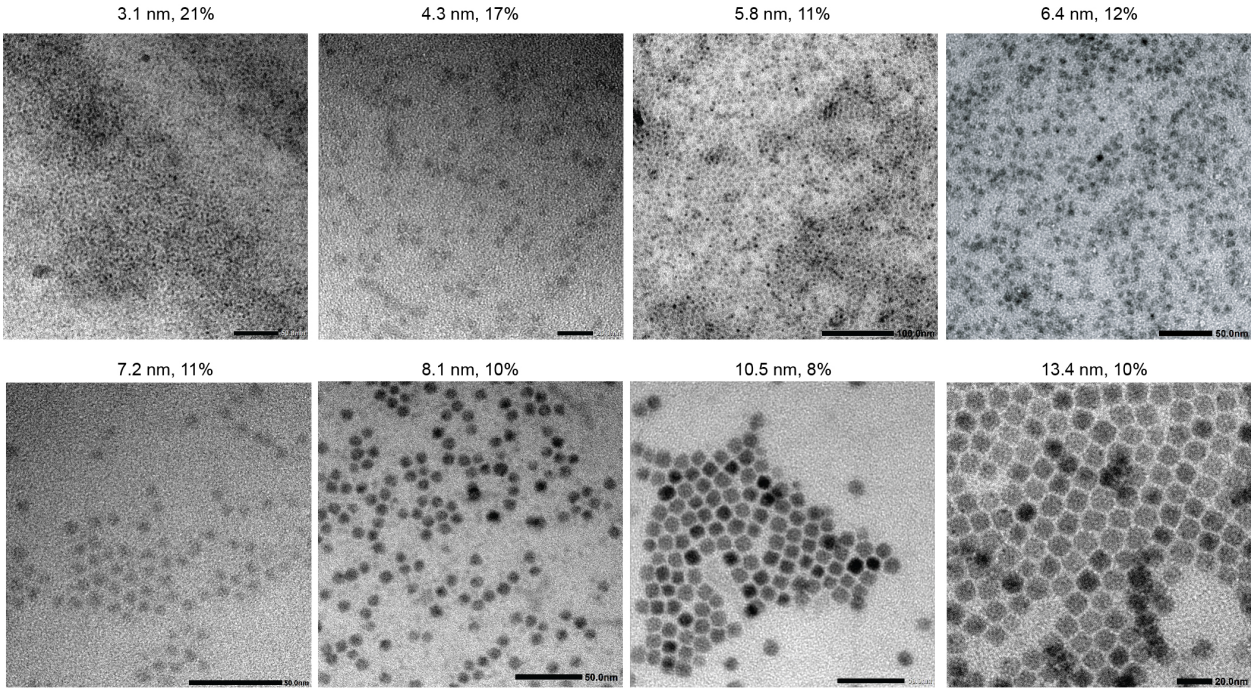

Supplementary Fig. 16 | Additional TEM images of 3 to 13 nm $CsPbBr_3$ QDs.

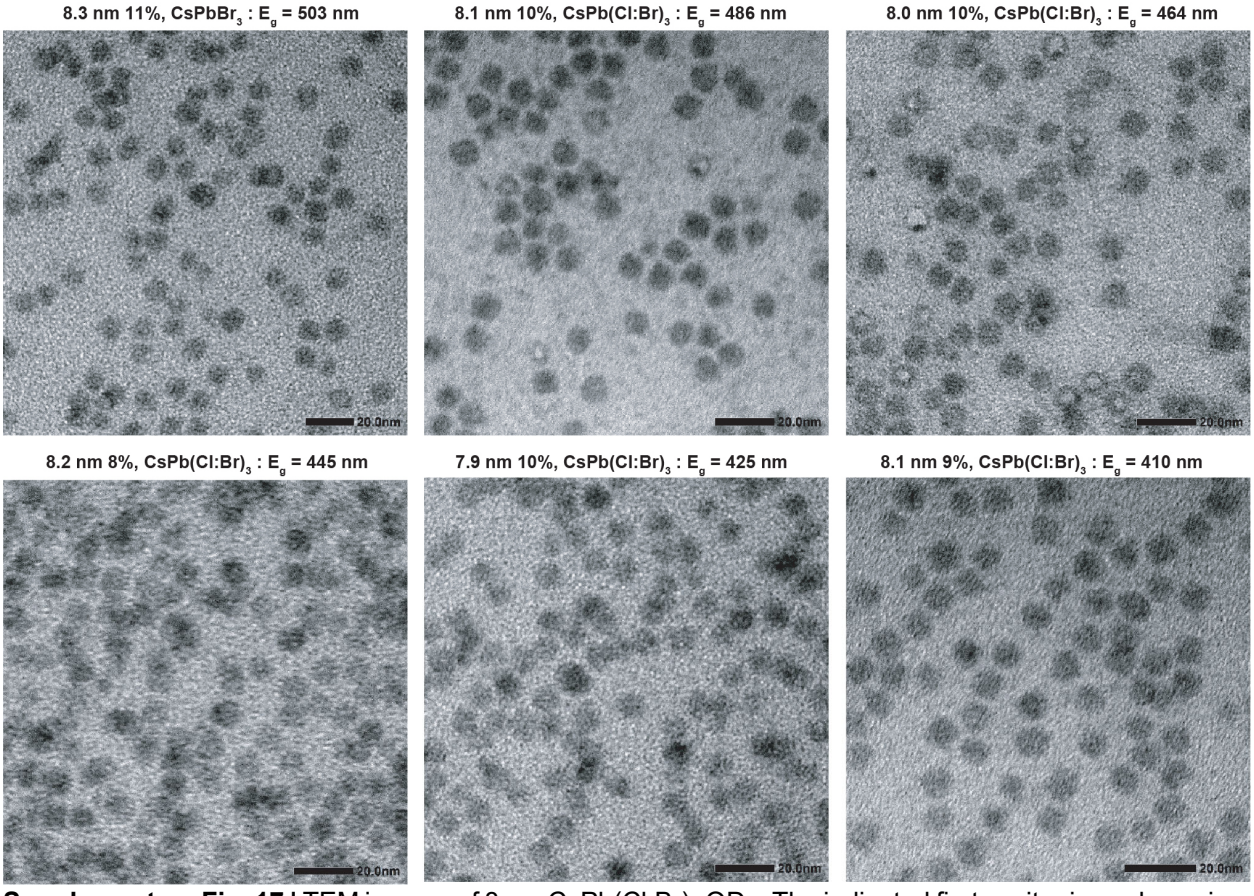

Supplementary Fig. 17 | TEM images of 8 nm $CsPb(Cl:Br)_3$ QDs. The indicated first excitonic peak maxima are adjustable by the Cl:Br ratio.

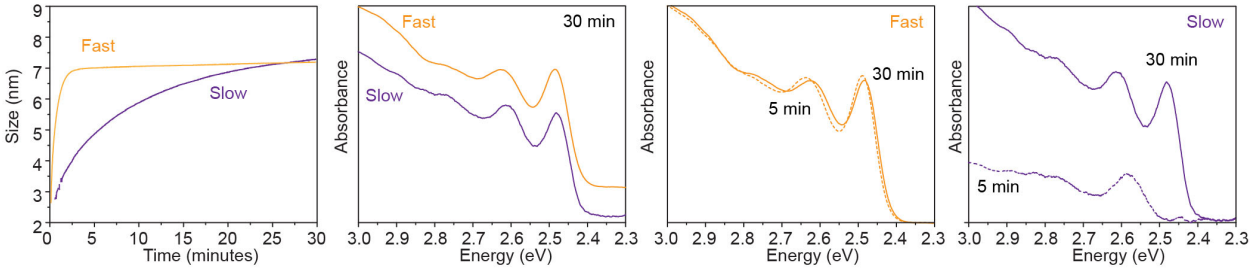

Supplementary Fig. 18 | Different $CsPbBr_3$ QDs obtained using a fast and slow reaction by optimizing the ratio and concentrations of Cs-TOPO, $PbBr_2$ and TOPO.

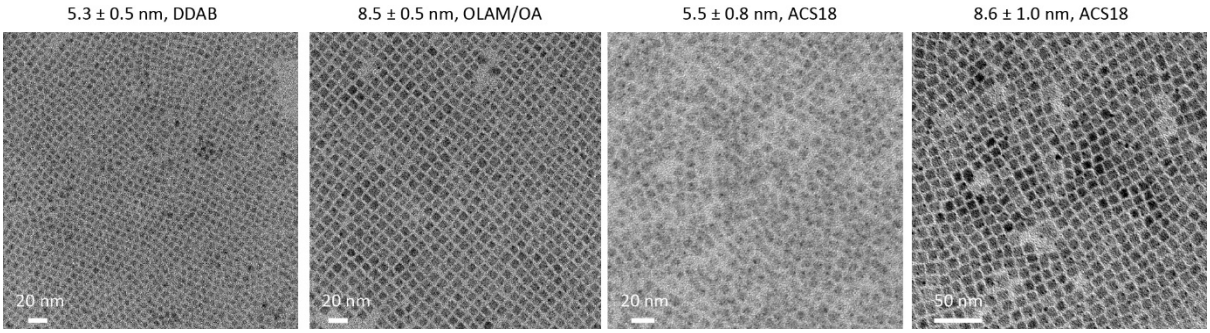

Supplementary Fig. 19 | Size and size-distributions of cuboidal reference $CsPbBr_3$ NCs, synthesized as described in our earlier publications[2,24].

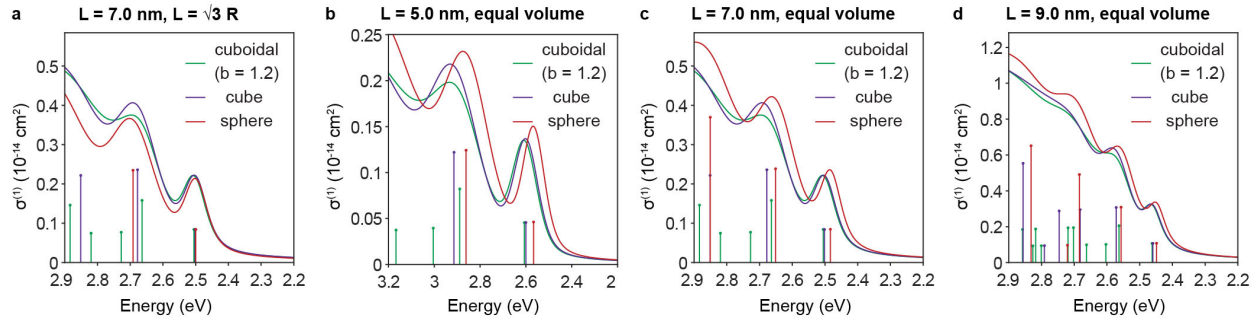

Supplementary Fig. 20 | Additional calculated absorption spectra for comparing cubic and spherical QD shapes. Here, the correspondence between a cube and a sphere was made either using $L = \sqrt{3}\,R$ for $L = 7.0$ nm (panel a) or based on matching their volume (panels b-d) for three sizes $L = 5.0$, 7.0, 9.0 nm. The same conclusion as in the main text Figure 2 is reached concerning the absorption spectra of the two geometries: for all sizes computed, the excitonic peaks are better defined for a spherical QD compared to the cubic one, notably for higher order transitions.

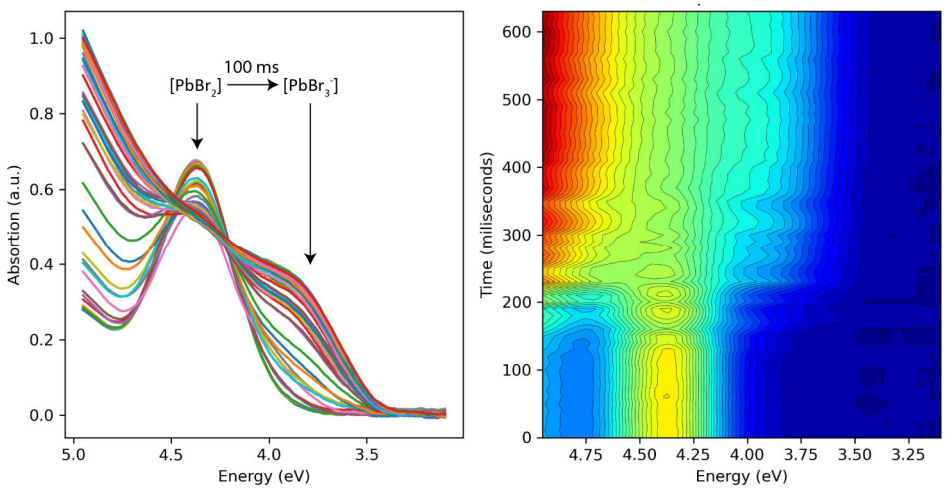

Supplementary Fig. 21 | Millisecond measurement of the formation of $PbBr_3^-$ complex upon the injection of Cs-DOPA into a $PbBr_2$[TOPO] solution.

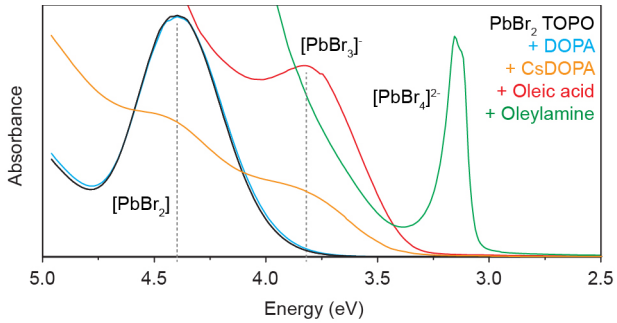

Supplementary Fig. 22 | Reaction of $PbBr_2$[TOPO] with several ligands including DOPA, oleic acid and oleylamine.

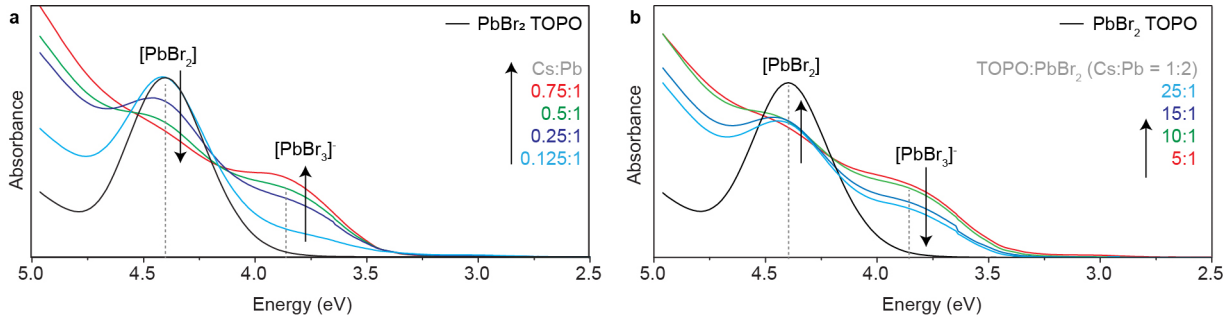

Supplementary Fig. 23 | Absorption spectra of $PbBr_2$ and $CsPbBr_3$ complexes directly after injection of Cs-DOPA with varying Cs:Pb and TOPO:$PbBr_2$ ratios. a, Cs[$PbBr_3$] concentration dependence with varying Cs:$PbBr_2$ ratio (maximum = 0.75). **b,** Cs[$PbBr_3$] concentration dependence with varying TOPO: $PbBr_2$ (minimum = 5).

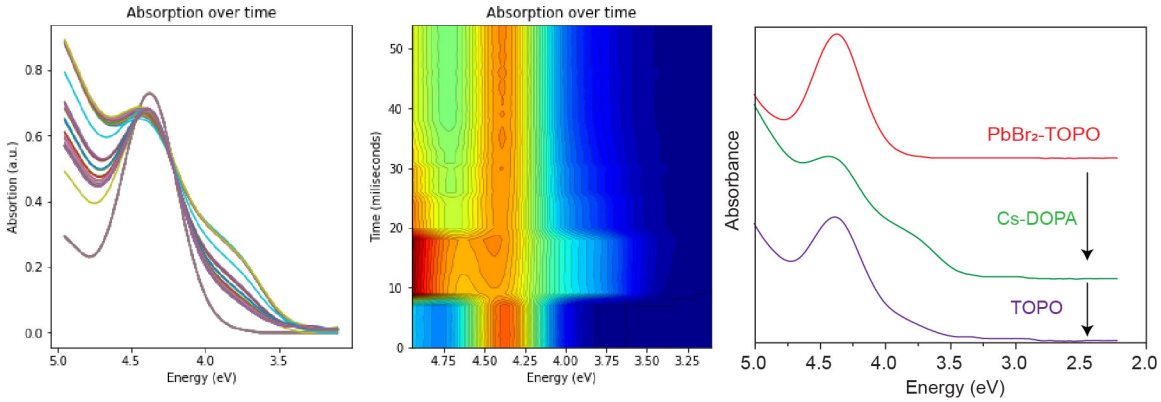

Supplementary Fig. 24 | Demonstration of reversibility of $PbBr_2$:Cs[$PbBr_3$] equilibrium obtained by a fast injection of additional TOPO after the initial Cs-DOPA injection.

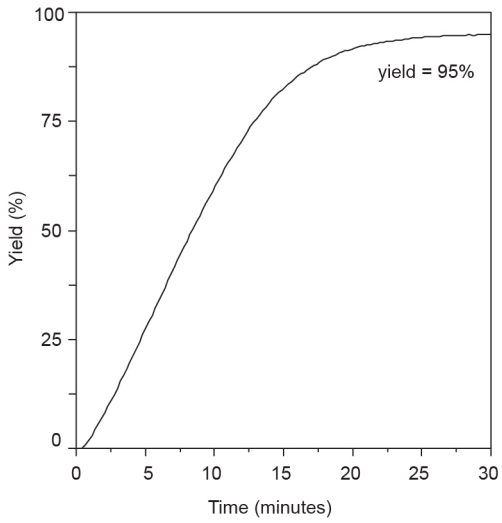

Supplementary Fig. 25 | Example of a typical reaction yield reaching near unity.

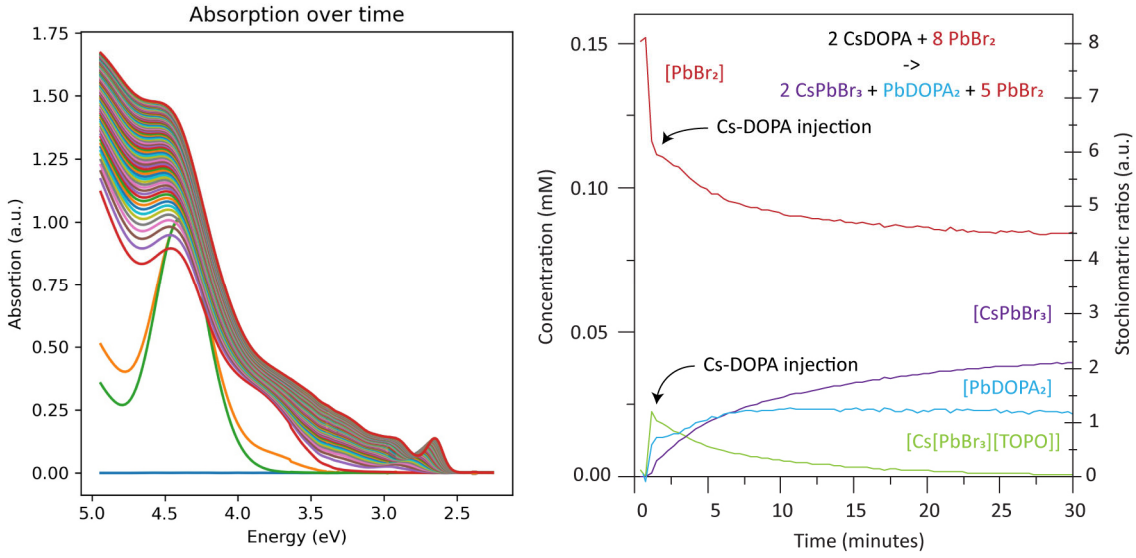

Supplementary Fig. 26 | Absorption spectra and concentration plot of reaction with excess of $PbBr_2$. At the end of the reaction no more $Cs[PbBr_3]$ is present and only 3/8th of the $PbBr_2$ is consumed, confirming that all formed $Cs[PbBr_3]$ is consumed for the formation of $CsPbBr_3$ QDs. These results evidence that the $PbBr_2$:$Cs[PbBr_3]$ equilibrium self-limits the available amount $Cs[PbBr_3]$ for both the initial nucleation, as well as the subsequent growth of $CsPbBr_3$ QDs.

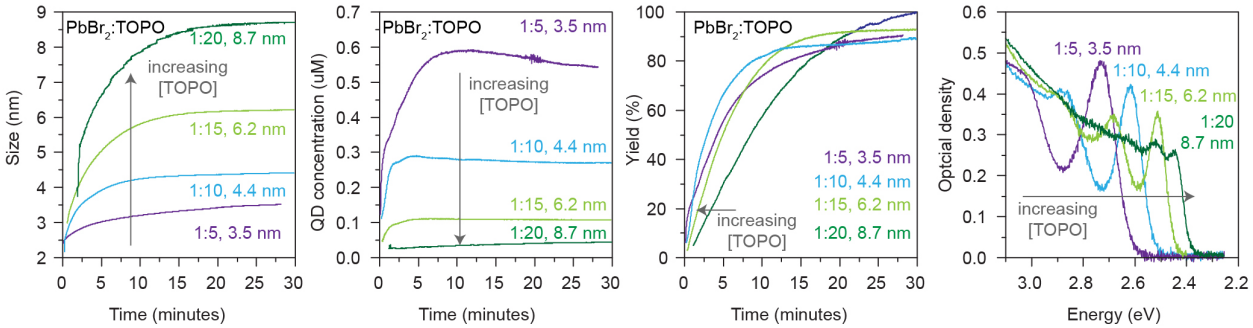

Supplementary Fig. 27 | Further details, including size, QD concentration, reaction yield and final optical absorption spectra of differently sized $CsPbBr_3$ QDs obtained with various concentrations of TOPO.

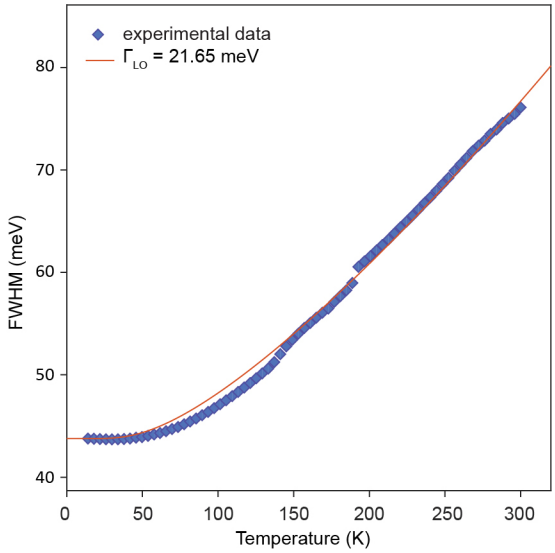

Supplementary Fig. 28 | Full width at half maximum (FWHM) of the lowest-energy absorption transition versus temperature for $L = 7.3$ nm. The experimental data were fitted using Gaussian line shape. Similar fit based on Voigt function closely reproduces the results from Gaussian fit function. The theoretical curve involves Gaussian-Lorentzian convolution to include some temperature-dependent effect. The fitted value $\Gamma_{LO} = 21.65$ meV using electron-phonon coupling with one LO-phonon mode as discussed **Supplementary Note 4.**

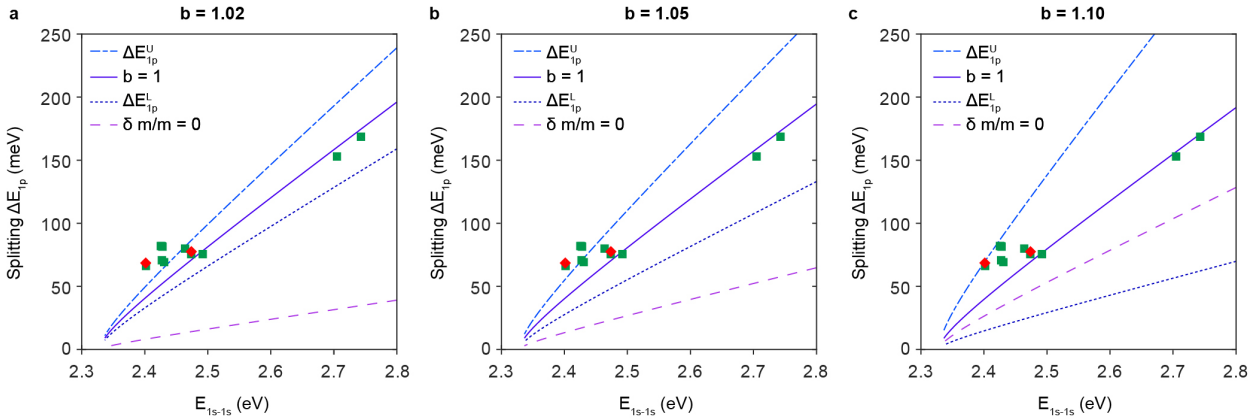

Supplementary Fig. 29 | Energy splitting ΔE_{1p} (meV) between the 1p-1p transitions versus the first absorption peak $E_{1s\text{-}1s}$ (eV). Experimental data points were extracted using second derivative (green square) or multi-Gaussian fit (red diamond) of the absorption spectra. The lines were obtained from theoretical calculations: upper bound ΔE_{1p}^{U} (light blue, dash dotted line), $\Delta E_{1p}^{\delta m/m}$ (solid blue) without shape anisotropy (i.e. $b = 1.00$), lower bound ΔE_{1p}^{L} (dark blue, dotted line) and ΔE_{1p}^{b} (purple dash line) without mass anisotropy (i.e. $\delta m/m = 0$). The dimensionless mass variation was fixed at $\delta m/m = 10\%$ for all three panels. The values of ΔE_{1p}^{b} clearly demonstrate that even using an excessive figure $b = 1.10$ for the extrinsic shape anisotropy, it is impossible to reproduce the measured splitting. This indicates other sources of anisotropy, those that are likely to be intrinsic to materials and syntheses. See **Supplementary Note 5** for more details on the theory and the discussion on these contributions to the p-state splitting.

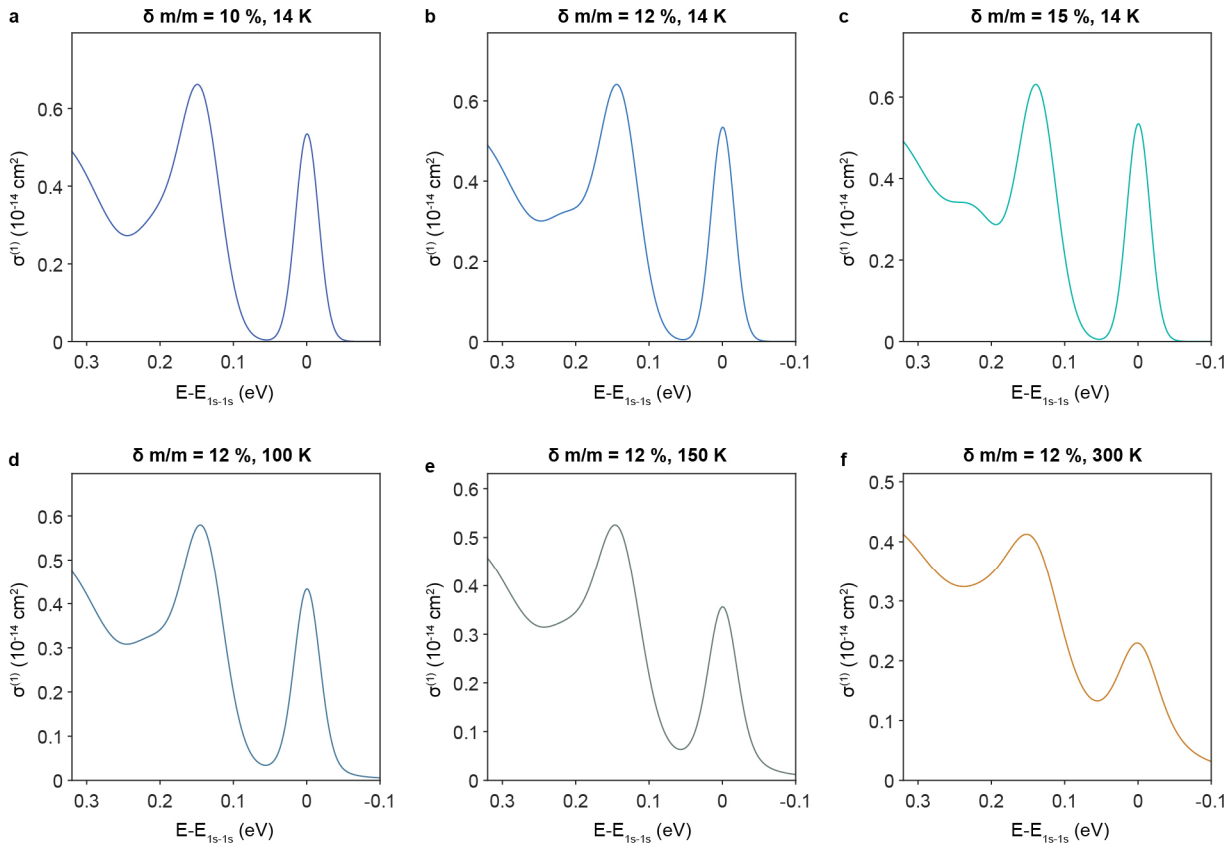

Supplementary Fig. 30 | Theoretical absorption spectra for $CsPbBr_3$ with the splitting in the 1p-1p transition at low temperature. The QD size is $L = 7.3$ nm for which the size dispersion was taken to be $\delta_{size} = 8\%$. The aspect ratio *b*, as discussed in **Supplementary Note 2,** was fixed 1.03 as obtained from SAXS measurements. The widths of the 1p states were set to be 75% of the estimated line shape outlined in **Supplementary Note 4** for the splitting to be visible. As the mass variation $\delta m/m$ increases from 10% to 12% and then 15%, the separation between the 1p-1p peaks grows bigger as manifested in the spectra in panels a-c at $T = 14$ K. Fixing $\delta m/m = 12\%$, the calculations with increasing temperature where $T =$ 100 K, 150 K and 300 K shows that the p-state splitting is no longer observable at room temperature due to thermal broadening.

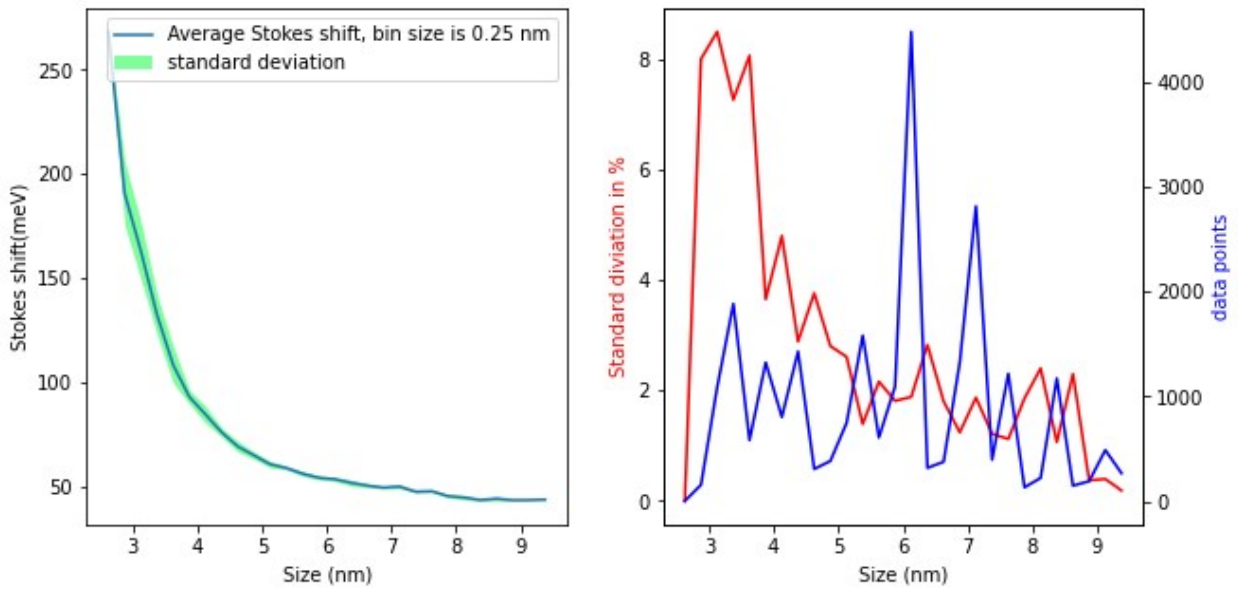

Supplementary Fig. 31 | Average Stokes shift and standard deviation calculation. Here, the Stokes shift data is binned in 0.25 nm parts. Each bin size can then be used to calculate an average Stokes shift for that size with its respective standard deviation.

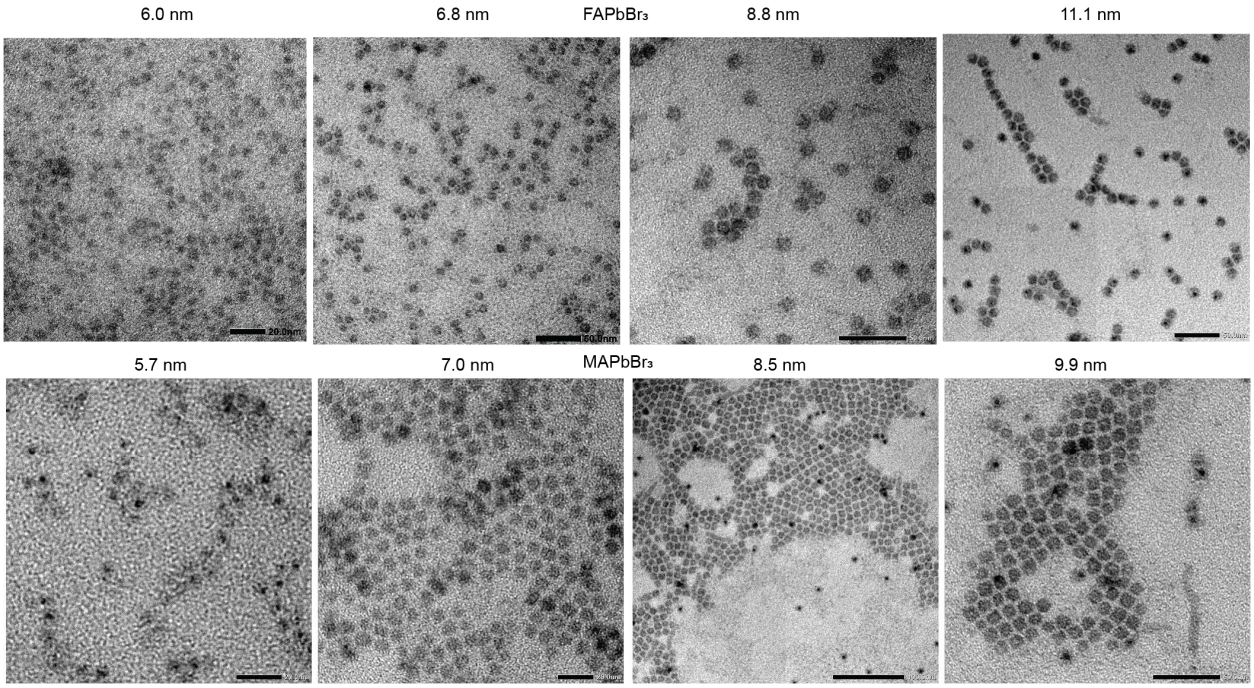

Supplementary Fig. 32 | Additional TEM images of $FAPbBr_3$ and $MAPbBr_3$ QDs.

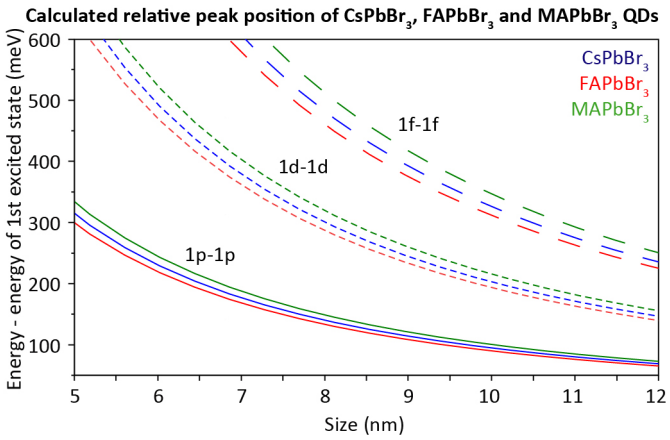

Supplementary Fig. 33 | Calculated relative absorption transition peak position of $CsPbBr_3$, $FAPbBr_3$ and $MAPbBr_3$ QDs as function of QD size, demonstrating relative peak position is independent of the A-site cation.

References

1. Akkerman, Q. A. *et al.* Nearly Monodisperse Insulator Cs_4PbX_6 (X = Cl, Br, I) Nanocrystals, Their Mixed Halide Compositions, and Their Transformation into $CsPbX_3$ Nanocrystals. *Nano Lett.* **17**, 1924-1930 (2017).
2. Krieg, F. *et al.* Monodisperse Long-Chain Sulfobetaine-Capped $CsPbBr_3$ Nanocrystals and Their Superfluorescent Assemblies. *ACS Cent. Sci.* **7**, 135-144 (2021).
3. Nguyen, T. P. T., Blundell, S. A. & Guet, C. One-Photon Absorption by Inorganic Perovskite Nanocrystals: A Theoretical Study. *Phys. Rev. B* **101**, 195414 (2020).
4. Nguyen, T. P. T., Blundell, S. A. & Guet, C. Calculation of the Biexciton Shift in Nanocrystals of Inorganic Perovskites. *Phys. Rev. B* **101**, 125424 (2020).
5. Yang, Z. *et al.* Impact of the Halide Cage on the Electronic Properties of Fully Inorganic Cesium Lead Halide Perovskites. *ACS Energy Lett.* **2**, 1621-1627 (2017).
6. Galkowski, K. *et al.* Determination of the Exciton Binding Energy and Effective Masses for Methylammonium and Formamidinium Lead Tri-Halide Perovskite Semiconductors. *Energy Environ. Sci.* **9**, 962-970 (2016).
7. Maes, J. *et al.* Light Absorption Coefficient of $CsPbBr_3$ Perovskite Nanocrystals. *J. Phys. Chem. Lett.* **9**, 3093-3097 (2018).
8. Almeida, G. *et al.* The Phosphine Oxide Route toward Lead Halide Perovskite Nanocrystals. *J. Am. Chem. Soc.* **140**, 14878-14886 (2018).
9. Protesescu, L. *et al.* Nanocrystals of Cesium Lead Halide Perovskites ($CsPbX_3$, X = Cl, Br, and I): Novel Optoelectronic Materials Showing Bright Emission with Wide Color Gamut. *Nano Lett.* **15**, 3692-3696 (2015).
10. Olivero, J. J. & Longbothum, R. L. Empirical Fits to the Voigt Line Width: A Brief Review. *J. Quant. Spectrosc. Radiat. Transfer* **17**, 233-236 (1977).
11. Ramade, J. *et al.* Exciton-Phonon Coupling in a $CsPbBr_3$ Single Nanocrystal. *Appl. Phys. Lett.* **112**, 072104 (2018).
12. Traoré, B. *et al.* Efficient and Accurate Calculation of Band Gaps of Halide Perovskites with the Tran-Blaha Modified Becke-Johnson Potential. *Phys. Rev. B* **99**, 035139 (2019).
13. Puppin, M. *et al.* Evidence of Large Polarons in Photoemission Band Mapping of the Perovskite Semiconductor $CsPbBr_3$. *Phys. Rev. Lett.* **124**, 206402 (2020).

14. Sakuma, T. *et al.* Low-Energy Excitation in $CsPbX_3$ (X=Cl, Br). *Solid State Ion.* **154-155**, 237-242 (2002).
15. Stoumpos, C. C. *et al.* Crystal Growth of the Perovskite Semiconductor $CsPbBr_3$: A New Material for High-Energy Radiation Detection. *Cryst. Growth Des.* **13**, 2722-2727 (2013).
16. López, C. A. *et al.* Crystal Structure Features of $CsPbBr_3$ Perovskite Prepared by Mechanochemical Synthesis. *ACS omega* **5**, 5931-5938 (2020).
17. Zhang, M. *et al.* Growth and Characterization of All-Inorganic Lead Halide Perovskite Semiconductor $CsPbBr_3$ Single Crystals. *CrystEngComm* **19**, 6797-6803 (2017).
18. Cottingham, P. & Brutchey, R. L. Depressed Phase Transitions and Thermally Persistent Local Distortions in $CsPbBr_3$ Quantum Dots. *Chem. Mater.* **30**, 6711-6716 (2018).
19. Brennan, M. C., Kuno, M. & Rouvimov, S. Crystal Structure of Individual $CsPbBr_3$ Perovskite Nanocubes. *Inorg. Chem.* **58**, 1555-1560 (2019).
20. Yu, Z.-L. *et al.* Oriented Tuning the Photovoltaic Properties of Γ-$RbGeX_3$ by Strain-Induced Electron Effective Mass Mutation. *J. Phys. D: Appl. Phys.* **50**, 465101 (2017).
21. Zhu, C. *et al.* Strain Engineering in Perovskite Solar Cells and Its Impacts on Carrier Dynamics. *Nat. Commun.* **10**, 815 (2019).
22. Kim, H.-S. & Park, N.-G. Importance of Tailoring Lattice Strain in Halide Perovskite Crystals. *NPG Asia Mater.* **12**, 78 (2020).
23. Burian, M. & Amenitsch, H. Dummy-Atom Modelling of Stacked and Helical Nanostructures from Solution Scattering Data. *IUCrJ* **5**, 390-401 (2018).
24. Cherniukh, I. *et al.* Perovskite-Type Superlattices from Lead Halide Perovskite Nanocubes. *Nature* **593**, 535-542 (2021).